

# Ne VIII in the warm-hot circumgalactic medium of FIRE-2 and FIRE-3 simulations and in observations

Nastasha A. Wijers,<sup>1\*</sup> Claude-André Faucher-Giguère,<sup>1</sup> Jonathan Stern,<sup>2</sup> Lindsey Byrne,<sup>1</sup> Imran Sultan<sup>1</sup>

<sup>1</sup>*CIERA and Department of Physics and Astronomy, Northwestern University, 1800 Sherman Ave, Evanston, IL 60201, USA*

<sup>2</sup>*School of Physics & Astronomy, Tel Aviv University, Tel Aviv 69978, Israel*

Accepted XXX. Received YYY; in original form ZZZ

## ABSTRACT

The properties of warm-hot gas around  $\sim L_*$  galaxies are highly uncertain, but can be studied with absorption lines from highly ionized metals. We have predicted Ne VIII column densities from FIRE-2 and FIRE-3 simulations of haloes with masses  $\sim 10^{12}$  and  $\sim 10^{13} M_\odot$ . Ne VIII in  $\sim 10^{12} M_\odot$  haloes traces the volume-filling, warm-hot gas phase. In  $\sim 10^{13} M_\odot$  haloes, the Ne VIII in the haloes is clumpier, and biased towards the cooler part of the warm-hot gas. We compare these predictions to observations at similar halo masses by Burchett et al. (2019) and Qu et al. (2023). We find that the scatter in the stellar-mass-halo-mass relation matters when estimating halo masses from stellar masses, especially at  $M_\star \gtrsim 10^{10.5} M_\odot$ . Compared to a small set of observed absorbers, the Ne VIII column densities seem to be too low in the FIRE models, as well as in other cosmological simulations from the literature. However, we can produce the highest measured column densities with analytical models if we assume the haloes have high gas fractions and metallicities. Therefore, the observations seem to be consistent with plausible CGM temperatures, metallicities, and gas masses, but it seems that self-consistently producing realistic galaxies and CGM is difficult.

**Key words:** galaxies: haloes – galaxies: groups: general – galaxies: formation – (galaxies:) quasars: absorption lines

## 1 INTRODUCTION

The circumgalactic medium, a halo of gas surrounding galaxies, plays an import role in galaxy formation and evolution (e.g., the review by Tumlinson et al. 2017). If this gas accretes onto the central galaxy, it can form stars. Conversely, cutting off accretion onto a central galaxy can quench it (e.g., the review by Faucher-Giguère & Oh 2023). This can occur due to the feedback from the central galaxy (stars and AGN), which can heat ISM gas and eject it into the CGM. It can also heat the CGM, and possibly generate outflows which escape the halo altogether (e.g., Mitchell & Schaye 2022; Hafen et al. 2020; Pandya et al. 2020; Muratov et al. 2017, 2015).

This means that understanding the CGM can help us understand the processes which regulate galaxy formation. However, we currently do not know how much mass there is in the CGM around  $L_*$  (halo mass  $\sim 10^{12} M_\odot$ ) galaxies (Werk et al. 2014). Haloes around this mass, roughly  $\sim 10^{12}$ – $10^{13} M_\odot$ , are interesting, as these haloes are where central galaxy quenching mostly occurs (e.g., Behroozi et al. 2019). This is the mass range we will investigate in this paper.

We have many observations of cool CGM gas ( $\sim 10^4$ – $10^5$  K) from UV absorption line observations (e.g., Tumlinson et al. 2017), from which we can infer its temperature, density, and metallicity, and mass. There are also many detections of O VI absorption. This can come from warmer gas at  $\sim 10^{5.5}$  K, but it can also trace cool, photo-ionized gas.

The warm/hot, virialized CGM gas phase is where CGM mass estimates are most uncertain (Werk et al. 2014). Its absorption and

emission lines are largely in the X-ray band (e.g., Perna & Loeb 1998; Hellsten et al. 1998; Chen et al. 2003; Cen & Fang 2006; Branchini et al. 2009), where absorption line detections are rare and do not often reach high significance (e.g., Nicastro 2016). There is a larger sample of X-ray observations of the Milky Way halo (e.g., Bregman & Lloyd-Davies 2007; Gupta et al. 2014; Miller & Bregman 2015; Gupta et al. 2017; Das et al. 2019), but as this is a single system, it can be difficult to draw conclusions about the CGM in general from these.

Planned and proposed future instruments such as the Athena X-IFU (Nandra et al. 2013; Barret et al. 2018), Arcus (Smith et al. 2016), LEM (Kraft et al. 2022), HUBS (Cui et al. 2020), and Lynx (The Lynx Team 2018) can give us the X-ray absorption and emission line data we need (e.g., Wijers et al. 2020; Wijers & Schaye 2022; Nelson et al. 2023). However, current X-ray instruments do not have the sensitivity and spectral resolution required to observe the CGM of a large set of  $\sim L_*$  haloes. Fast radio burst dispersion measures (e.g., McQuinn 2014) and measurements of the Sunyaev-Zel’dovich (SZ) effect (e.g., the review by Mroczkowski et al. 2019) could also provide future constraints on the CGM ionized gas content, but robust measurements of the CGM content of Milky-Way-like haloes will require larger samples of localized FRBs (e.g., Ravi 2019) or instrumental improvements for SZ measurements such as a higher spatial resolution (Mroczkowski et al. 2019).

Therefore, in this paper, we focus on an extreme UV (EUV) absorption line: the Ne VIII doublet at 770, 780 Å. Burchett et al. (2019) and Qu et al. (2023) completed surveys for Ne VIII absorption in quasar spectra, and obtained galaxy observations along the quasar sightlines. This allows them to associate the absorbers with the haloes

\* E-mail: nastasha.wijers@northwestern.edu

of specific galaxies. Ne VIII traces  $\approx 10^{5.6}-10^{6.2}$  K gas in collisional ionisation equilibrium (CIE). This makes it a good candidate to trace the warm/hot, volume-filling gas in  $\sim 10^{12} M_{\odot}$  haloes (e.g., [Verner et al. 1994](#)).

We compare this data to predictions from a set of FIRE-3 simulations with different AGN feedback models and FIRE-2 simulations (without AGN) to test whether the warm/hot CGM of the FIRE  $M_{\text{vir}} \sim 10^{12}$  and  $\sim 10^{13} M_{\odot}$  haloes is consistent with the observations of [Burchett et al. \(2019\)](#) and [Qu et al. \(2023\)](#). We also test how sensitive the Ne VIII column densities are to the differences between the models, and check whether the simulations can simultaneously match the properties of galaxies and their haloes in the mass range where they are quenched.

In §2, we describe the FIRE-2 and FIRE-3 simulations we analyse, and how we predict column densities from them. Next, in §3, we explore the properties of Ne VIII in the haloes we study. In §4, we then describe how the FIRE predictions compare to the observations. Next, we explore a simple analytical model for Ne VIII column densities in §5. In §6, we compare our results to others in the literature. Finally, we summarize our results in §7. For an analysis of the intrinsic properties of galaxies and the CGM using the FIRE-3 physics models, see [Byrne et al. \(in prep.\)](#) and [Sultan et al. \(in prep.\)](#), respectively.

We use a flat  $\Lambda$ CDM cosmology, with  $h \approx 0.7$ ,  $\Omega_{\Lambda} \approx 0.7$ , and  $\Omega_m \approx 0.3$ . We analyse each simulation using the parameter set it was run with.

## 2 METHODS

In this work, we analyse simulations run with four different physics models: one ‘core’ FIRE-2 model, and three FIRE-3 models. The FIRE-3 models have no AGN feedback, AGN feedback without cosmic rays, and AGN feedback with cosmic rays. We initially focused our analysis on the FIRE-3 models. However, we found the Ne VIII column densities in these models were somewhat low compared to observations. Based on the findings of [Ji et al. \(2020\)](#), we decided to check whether a FIRE-2 model would fare better.

Below, we describe these simulations in more detail, and briefly explain how we predict column densities from them.

### 2.1 The FIRE-2 simulations

The FIRE-2 (Feedback In Realistic Environments<sup>1</sup>) simulations are described in detail in [Hopkins et al. \(2018b\)](#). The simulations use the meshless finite-mass (MFM) magneto-hydrodynamics solver ([Hopkins 2015a](#)), in the GIZMO<sup>2</sup> code ([Hopkins 2015b](#)).

In the FIRE-2 simulations, 11 elements are explicitly tracked, including neon. The radiative cooling and heating calculations ([Hopkins et al. 2018b](#)) include processes relevant to the cool and cold ISM, such as cooling from molecules and fine-structure lines. The cooling and heating processes are applicable to temperatures of  $10-10^{10}$  K. For temperatures  $> 10^4$  K, metal-line cooling follows [Wiersma et al. \(2009\)](#). The effects of ionizing photons from both a [Faucher-Giguère et al. \(2009\)](#) background and stars in the simulations are included. For radiation from stars, a radiative transfer method with a self-shielding approximation is used (LEBRON; [Hopkins et al. 2012, 2018b](#)).

Star formation can occur in gas if it is (1) self-gravitating (the potential energy is larger than the thermal and kinetic energy combined), (2) self-shielding (it contains molecular gas), (3) Jeans-unstable (the thermal Jeans mass is smaller than the resolution element mass), and (4) has a minimum density  $n_H > 10^3 \text{ cm}^{-2}$ . The star formation rate is then simply the molecular gas density over the free-fall time of the resolution element. Star particles represent a single-age stellar population, and have the mass and element abundances of the gas particles they formed from.

The feedback from each single-age stellar population is taken from STARBURST99 ([Leitherer et al. 1999](#)), assuming a [Kroupa \(2001\)](#) stellar initial mass function and a stellar mass range of  $0.1-100 M_{\odot}$ . This includes supernova rates, and abundances, mass, and energy in supernovae and stellar winds. The injected supernova momentum and energy depend on the Sedov-Taylor solution for the explosion, given the density and mass of the surrounding gas ([Hopkins et al. 2018a; Martizzi et al. 2015](#)).

There are various additional options in the FIRE-2 simulations. In particular, the simulations we analyse include a prescription for subgrid metal diffusion ([Hopkins et al. 2018b; Colbrook et al. 2017](#)). The FIRE-2 simulations we analyse have redshift 0 main halo masses of  $\sim 10^{12} M_{\odot}$ , and are listed in Tab. 1.

### 2.2 The FIRE-3 simulations

The FIRE-3 simulations are a set of simulations run with different physics models and initial conditions using the FIRE-3 code ([Hopkins et al. 2023](#)). Much of the modeling is the same as in the FIRE-2 simulations, with some updates. Compared to FIRE-2, FIRE-3 galaxy stellar masses in  $\sim 10^{12} M_{\odot}$  haloes tend to be lower ([Hopkins et al. 2023](#)).

The FIRE-3 simulations include magnetic fields ([Hopkins & Raives 2016; Hopkins 2016](#)) by default, including the FIRE-3 simulations we analyse, and unlike our FIRE-2 sample. Subgrid metal diffusion is also included by default; this was already included in the FIRE-2 simulations we analyse. A number of models were updated with the change from FIRE-2 to FIRE-3. For example, the UV/X-ray background was updated to that of [Faucher-Giguère \(2020\)](#). When calculating ion fractions, we will use the tables produced by [Ploechinger & Schaye \(2020\)<sup>3</sup>](#), who also assumed a [Faucher-Giguère \(2020\)](#) UV/X-ray background. Stellar evolution and feedback modeling were also updated, and the star formation criteria from FIRE-2 were adjusted for FIRE-3: the gas must be (1) self-gravitating, (2) Jeans-unstable, and (3) converging or not diverging too rapidly.

We consider, in particular, a set of three FIRE-3 physics models. The first includes no AGN feedback (noBH), the second includes AGN feedback without cosmic rays (AGN-noCR), and the third includes AGN feedback with cosmic rays (AGN-CR). The FIRE-2 model contains neither black holes, nor cosmic rays, so we will label it ‘FIRE-2 noBH’. Note that the AGN-CR model contains cosmic rays from AGN and supernovae, while the other models do not contain cosmic rays from any source. For the FIRE-3 simulations, we consider haloes with redshift 0 halo masses of  $\sim 10^{12} M_{\odot}$  (m12 haloes). Unlike for the FIRE-2 model, we also include more massive m13 haloes, with redshift 0 halo masses  $\sim 10^{13} M_{\odot}$ .

In the AGN-noCR and AGN-CR models, black holes (BHs) are stochastically seeded from star-forming gas, especially at high surface

<sup>1</sup> See the FIRE project website: <https://fire.northwestern.edu/>

<sup>2</sup> The public GIZMO version is available at <http://www.tapir.caltech.edu/%7Ephopkins/Site/GIZMO.html>.

<sup>3</sup> The tables are available at <https://dataverse.harvard.edu/dataset.xhtml?persistentId=doi:10.7910/DVN/GR3L5N>. We specifically use the UVB\_dust1\_CR1\_G1\_shield1.hdf5 table.

densities and low metallicities (Wellons et al. 2023; Hopkins et al. 2018b). They merge if they are close together and gravitationally bound. The black hole accretion model is described by Hopkins et al. (2018b) and Wellons et al. (2023).

AGN feedback follows Wellons et al. (2023), with the parameters given by Byrne et al. (in prep.). Radiative feedback is injected at a rate of 0.1 times the accretion rate. Winds are injected (Torrey et al. 2020; Su et al. 2021) at a fixed velocity of  $3000 \text{ km s}^{-1}$ , parallel to the BH angular momentum (Hopkins et al. 2016). The wind mass injection rate is equal to the black hole accretion rate. In the AGN-CR model, jets are modelled by adding CRs to the created wind resolution elements, with an energy efficiency of  $10^{-3}$  relative to the BH mass accretion rate.

In the AGN-CR simulations, the cosmic ray (CR) model evolves the CR spectrum for protons and electrons (Hopkins 2023; Hopkins et al. 2022b,a, 2020; Chan et al. 2019). Specifically, the modified external driving model in §5.3.2 of Hopkins et al. (2022c) is used. CRs are injected by supernova explosions and stellar winds, making up 10% of the initial kinetic energy in both, and by AGN as described above.

### 2.3 The simulation sample

In the previous two sections, we described the physics models we examine in this work. Here, we describe which initial conditions (ICs) and resolutions we use. We give an overview in Table 1.

We analyse a set of cosmological zoom simulations of haloes with masses  $\sim 10^{12} M_{\odot}$  (m12) and  $\sim 10^{13} M_{\odot}$  (m13). References for the individual simulations are given below; many of the FIRE-3 simulations have not yet been formally described in a published paper<sup>4</sup>. The FIRE-3 physics models we analyse here match those analysed by Sultan et al. (in prep.) and Byrne et al. (in prep.).

The set of FIRE-2 simulations we analyse comes from the public release of FIRE-2 data by Wetzel et al. (2023). We specifically consider the haloes with redshift 0 masses of  $\sim 10^{12} M_{\odot}$  in the ‘core’ suite<sup>5</sup>. These haloes were selected from a cosmological volume based on their mass, and being relatively isolated from haloes of similar or higher masses.

The m12m FIRE-2 simulation we analyse was first presented by Hopkins et al. (2018b), and the m12b, m12c, and m12z simulations we analyse were first presented in Garrison-Kimmel et al. (2019). The FIRE-2 m12i simulation we analyse here is very similar to the one first presented by Wetzel et al. (2016), and the m12f halo to that presented by Garrison-Kimmel et al. (2017). The m12b, m12c, m12f, m12i, and m12m haloes are part of the ‘Latte Suite’, selected to have redshift zero halo masses similar to that of the Milky Way,  $M_{200m} = 1 - 2 \times 10^{12} M_{\odot}$ <sup>6</sup>, while m12z was selected to have a slightly lower halo mass (Garrison-Kimmel et al. 2019). Samuel et al. (2020) first presented the m12w and m12r simulations we analyse. These haloes were selected in the same halo mass range as the Latte suite, but with the additional requirement that they have LMC-like subhaloes in the initial dark-matter-only simulations.

For most of the FIRE-3 haloes, there are not yet papers describing them. The m12 initial conditions are the same as those above,

albeit sometimes at a different resolution. The FIRE-3 noBH m12i simulation was presented by Hopkins et al. (2023). At least for a subset of the haloes we analyse here, simulations using all three of the FIRE-3 physics models will be presented by Byrne et al. (in prep., galaxy properties) and Sultan et al. (in prep., circumgalactic medium properties).

We list the halo mass, virial radius, and stellar mass of the central galaxy of each simulation in Tab. 1. We show these values at redshifts 0.5 and 1.0, since we analyse simulations between these redshifts. This range was selected to roughly match the redshift range searched by Burchett et al. (2019); the Qu et al. (2023) data cover a smaller redshift range. We similarly analysed m12 and m13 haloes, since the Burchett et al. (2019) galaxies likely reside in haloes of roughly these masses (see §4.1). We use the Bryan & Norman (1998) halo virial mass definition. In §2.4, we will describe how we calculated the galaxy and halo positions and masses.

For each physics model and halo mass category, we analyse a set of simulations run at similar resolutions, to ensure these samples are internally consistent. For a given halo mass range, physics model, and resolution scale, we analysed the haloes from simulations which had reached redshift 0.5. This ensured each simulation covered our target redshift range 0.5–1.0. Within this range, we specifically analyse simulation outputs at redshifts 0.5, 0.6, 0.7, 0.8, 0.9, and 1.0.

Of our haloes, only m12f was run for all m12 physics models, and only m13h113 and m13h206 reached redshift 0.5 for all three m13 physics models. In comparisons between physics models, we will therefore often focus on these haloes, which we call our ‘clean sample’.

### 2.4 Finding and centering our haloes

The haloes we analyse in this paper are the main haloes in each zoom-in volume. We find the halo centers using a shrinking-spheres method (Power et al. 2003), starting at the center of mass of the zoom-in region. We use all zoom region resolution elements (high-resolution dark matter, gas, stars, and black holes if included) to determine the halo center. We then find the halo virial radius and mass using the Bryan & Norman (1998) mean enclosed halo density.

For the central galaxy stellar masses (Table 1), we first find the galaxy center by taking all stellar resolution elements within  $0.3 R_{\text{vir}}$  of the halo center, then recalculating the shrinking spheres center using only this stellar mass. We then measure the stellar mass within  $0.1 R_{\text{vir}}$  of the galaxy center.

### 2.5 Ion abundance calculation

As mentioned above, we use the Ploekinger & Schaye (2020) tables to calculate the ion fractions. We do not include the effect of dust depletion. (This is expected to be small at the densities and temperatures we are interested in.) These use the same photo-ionizing UV/X-ray background as assumed for the radiative cooling in the FIRE-3 simulations we study, and the same assumptions of ionization equilibrium.

We interpolate these tables linearly (for ion fraction and redshift) and linearly in log space (for temperature, density, and metallicity) to calculate ion fractions for a given resolution element. The total mass of ions in that resolution element is then simply the ion fraction multiplied by the resolution element mass and neon mass fraction.

<sup>4</sup> Note that this work is *not* the appropriate reference for these simulations.

<sup>5</sup> One minor difference is that the m12f and m12i haloes were simulated using the Wetzel et al. (2023, §2.4.1) code update. The effect of this difference should be minimal.

<sup>6</sup>  $M_{200m}$  is the mass enclosed within a sphere with a mean density 200 times the cosmic mean matter density at the halo redshift.

**Table 1.** The FIRE-2 and FIRE-3 simulations analysed in this work. We show initial conditions (ICs), physics model, resolution (for gas mass resolution elements), and the halo mass, stellar mass, and virial radius for redshifts 1.0 and 0.5. References for these simulations are given in the text.

ICs	model	resolution [M <sub>⊙</sub> ]	z = 1.0			z = 0.5		
			M <sub>vir</sub> [M <sub>⊙</sub> ]	M <sub>★</sub> [M <sub>⊙</sub> ]	R <sub>vir</sub> [pkpc]	M <sub>vir</sub> [M <sub>⊙</sub> ]	M <sub>★</sub> [M <sub>⊙</sub> ]	R <sub>vir</sub> [pkpc]
clean sample								
m12f	FIRE-3 AGN-CR	6e4	6.3e11	3.5e9	135	1.0e12	3.9e9	200
m12f	FIRE-3 AGN-noCR	7e3	6.6e11	5.6e9	137	1.0e12	8.5e9	201
m12f	FIRE-2 noBH	7e3	7.2e11	9.6e9	141	1.1e12	2.4e10	203
m12f	FIRE-3 noBH	7e3	6.8e11	4.0e9	138	9.9e11	6.7e9	199
m13h113	FIRE-3 AGN-CR	3e5	4.9e12	2.9e10	263	7.4e12	3.6e10	386
m13h113	FIRE-3 AGN-noCR	3e4	5.3e12	3.4e10	270	8.1e12	8.9e10	398
m13h113	FIRE-3 noBH	3e5	5.6e12	1.0e11	276	8.2e12	2.6e11	400
m13h206	FIRE-3 AGN-CR	3e5	3.9e12	3.8e10	244	5.7e12	4.3e10	354
m13h206	FIRE-3 AGN-noCR	3e4	4.3e12	4.8e10	252	6.1e12	1.2e11	362
m13h206	FIRE-3 noBH	3e5	4.3e12	1.2e11	253	6.1e12	2.2e11	363
full sample								
m12b	FIRE-3 AGN-noCR	7e3	6.0e11	4.5e9	132	1.1e12	8.0e9	205
m12b	FIRE-2 noBH	7e3	6.8e11	2.5e10	138	1.2e12	4.7e10	212
m12c	FIRE-2 noBH	7e3	6.0e11	5.1e9	132	6.9e11	1.9e10	176
m12i	FIRE-3 AGN-CR	6e4	7.5e11	4.1e9	143	6.9e11	5.1e9	176
m12i	FIRE-3 AGN-noCR	7e3	7.8e11	4.9e9	144	7.3e11	8.1e9	179
m12i	FIRE-2 noBH	7e3	8.4e11	1.0e10	149	8.3e11	2.7e10	187
m12m	FIRE-3 AGN-CR	6e4	6.5e11	5.1e9	136	8.4e11	8.6e9	188
m12m	FIRE-3 AGN-noCR	7e3	6.3e11	3.5e9	135	9.9e11	6.9e9	199
m12m	FIRE-2 noBH	7e3	8.1e11	5.3e9	147	1.1e12	2.7e10	206
m12q	FIRE-3 AGN-CR	6e4	8.1e11	3.1e9	147	1.2e12	3.8e9	209
m12q	FIRE-3 AGN-noCR	7e3	8.3e11	4.9e9	148	1.1e12	7.3e9	209
m12q	FIRE-3 noBH	7e3	8.3e11	5.1e9	148	1.2e12	9.2e9	212
m12r	FIRE-3 AGN-noCR	7e3	2.8e11	2.0e9	102	3.5e11	3.1e9	139
m12r	FIRE-2 noBH	7e3	2.9e11	2.6e9	103	3.5e11	4.6e9	139
m12r	FIRE-3 noBH	7e3	2.8e11	1.6e9	101	3.5e11	2.7e9	139
m12w	FIRE-3 AGN-noCR	7e3	3.8e11	3.5e9	112	8.2e11	6.3e9	185
m12w	FIRE-2 noBH	7e3	4.1e11	3.6e9	115	8.7e11	1.1e10	188
m12w	FIRE-3 noBH	7e3	3.8e11	2.4e9	112	7.6e11	3.4e9	180
m12z	FIRE-2 noBH	4e3	3.2e11	9.1e8	107	5.2e11	2.7e9	160
m12z	FIRE-3 noBH	4e3	2.8e11	6.8e8	103	4.6e11	8.0e8	153
m13h002	FIRE-3 AGN-CR	3e5	1.2e13	2.7e10	353	1.7e13	3.7e10	513
m13h002	FIRE-3 noBH	3e5	1.5e13	1.4e11	379	2.2e13	2.3e11	552
m13h007	FIRE-3 AGN-CR	3e5	7.5e12	4.1e10	304	1.2e13	4.7e10	457
m13h007	FIRE-3 noBH	3e5	8.4e12	9.7e10	316	1.4e13	1.6e11	477
m13h009	FIRE-3 AGN-CR	3e5	1.9e13	3.2e10	418	2.5e13	3.6e10	584
m13h029	FIRE-3 AGN-CR	3e5	8.5e12	3.7e10	318	1.0e13	5.2e10	433
m13h029	FIRE-3 noBH	3e5	9.1e12	1.3e11	324	1.2e13	3.0e11	453
m13h037	FIRE-3 AGN-CR	3e5	1.4e13	4.8e10	374	1.9e13	5.9e10	531
m13h223	FIRE-3 noBH	3e5	1.6e13	1.1e11	395	2.1e13	2.5e11	546
m13h236	FIRE-3 AGN-CR	3e5	5.1e12	2.4e10	268	7.2e12	2.9e10	383
m13h236	FIRE-3 noBH	3e5	6.0e12	1.1e11	282	8.3e12	2.2e11	401

## 2.6 Column density calculation

Given the number of ions in each resolution element, we now want to calculate the column density along various lines of sight. We do this by creating ‘column density maps’. We first define a volume and a line-of-sight direction. For the volume, we use a cube with side lengths (diameter) of  $4 R_{\text{vir}}$ , centered on the halo center. For the line-of-sight directions, we simply use the  $x$ -,  $y$ -, and  $z$ -axes of the simulation. We note that these directions are random with respect to the galaxy and halo orientation.

We divide the plane perpendicular to the line of sight into pixels of size  $(3 \text{ pkpc})^2$ . We then distribute the ions in each resolution element in the volume across these pixels based on each resolution

element’s position and size (SPH smoothing length). We assume the ion distribution in each resolution element is described by a Wendland C2 kernel (Wendland 1995). Figs. 1 and 2 show examples of these column density maps.

## 3 NE VIII IN FIRE

### 3.1 Column densities and clumpiness

We start our analysis by considering how Ne VIII is distributed in the FIRE haloes. To do this, we show images of some representative example m12 and m13 haloes in Figs. 1 and 2, respectively. For each



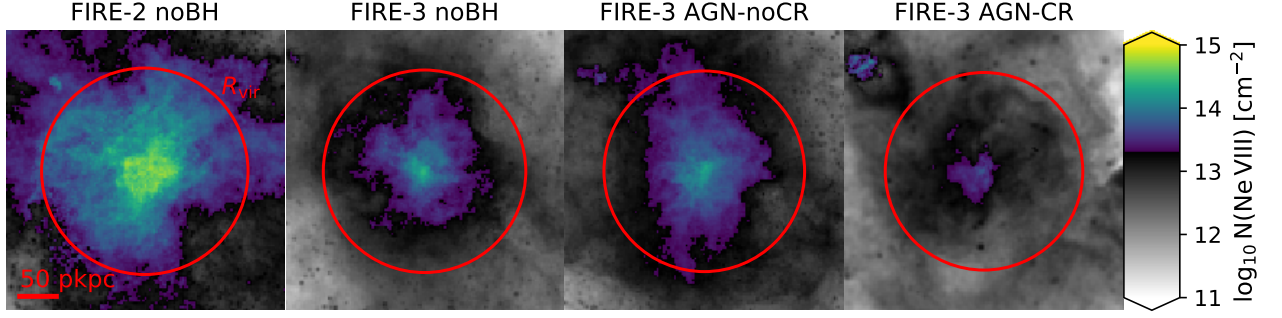


**Figure 1.** Ne VIII column density images for the four different physics models applied to the m12f initial conditions. These images are all at  $z = 1.0$ . The color scale switches from black and white to colors at a column density of  $10^{13.3} \text{ cm}^{-2}$ , the minimum column density Burchett et al. (2019) are sensitive to. The different panels show the same physical area; the red circles show each halo’s virial radius. The Ne VIII is distributed fairly smoothly within the m12 haloes.

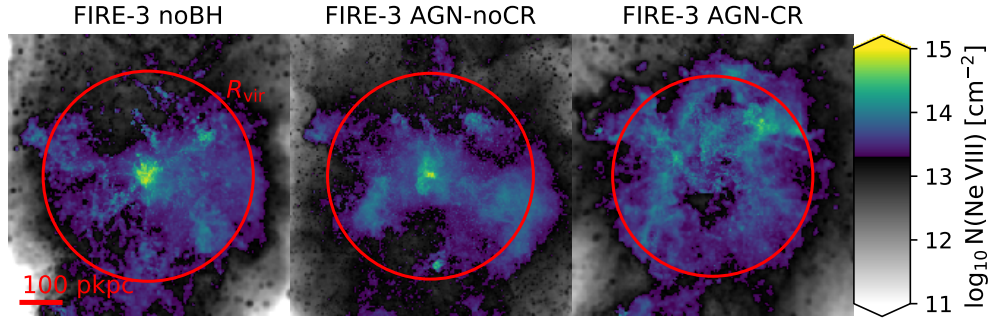


**Figure 2.** As Fig. 1, but for the m13h113 halo run with the three physics models. The Ne VIII in m13 haloes has a clumpier distribution.

halo mass sample, we show one halo, simulated using the different labelled physics models. These plots show the simulations at  $z = 1.0$ , with the line of sight along the  $z$ -axis. All column densities are measured to  $2 R_{\text{vir}}$  in either direction along the line of sight from the halo center. This is a subset of the images we will measure column density profiles from below.

Comparing the m12 and m13 haloes, the Ne VIII in the m12 haloes is fairly smoothly distributed, while this ion has a clumpier distribution in the m13 haloes. Differences between the panels for the different physics models reflect some broader differences, but some of these differences are just a coincidence for these haloes and this particular redshift.

For the m12 haloes, the FIRE-2 noBH model does more broadly predict higher column densities than the FIRE-3 models, and the FIRE-3 noBH and AGN-noCR models do predict similar column density profiles across haloes and redshifts. The FIRE-3 AGN-CR model tentatively seems to predict lower column densities than the other two FIRE-3 models, but with only two haloes for this physics model, this is somewhat uncertain. In general, the FIRE-3 noBH and AGN-noCR models also predict similar column densities in m13 haloes, while FIRE-3 AGN-CR predicts lower column densities in the halo center. Note that the ‘hole’ in the center of the m13h113 FIRE-3 AGN-CR image is not a common feature in the m13 AGN-CR model.

We explore the clumpiness of the m12 and m13 haloes in more detail in Fig. 3. We show all the haloes from our sample, and highlight the haloes and redshift from Figs. 1 and 2 in colors. We measure the

volume-weighted Ne VIII ‘smoothness’ using the clumping factor

$$f_{c,v} = \frac{\sum_i V_i n_{\text{Ne VIII},i}^2}{\sum_i V_i n_{\text{Ne VIII},i}} \frac{(\sum_i V_i)^2}{(\sum_i V_i n_{\text{Ne VIII},i})^2} \quad (1)$$

$$= \frac{\sum_i \mathcal{N}_{\text{Ne VIII},i} n_{\text{Ne VIII},i}}{\sum_i \mathcal{N}_{\text{Ne VIII},i}} \frac{\sum_i V_i}{\sum_i V_i n_{\text{Ne VIII},i}},$$

where we sum over resolution elements  $i$ , each with volume  $V_i$ , Ne VIII number density  $n_{\text{Ne VIII},i}$ , and containing  $\mathcal{N}_{\text{Ne VIII},i}$  Ne VIII ions. We note that this volume-weighted clumping factor  $f_{c,v}$  is the same as the Ne VIII-weighted Ne VIII density divided by the volume-weighted Ne VIII density.

In order to keep our range of values limited (between 0 and 1), we show  $f_{\text{fill}} = 1 / f_{c,v}$  in Fig. 3. We note that this can be interpreted as the fraction of the CGM volume occupied by Ne VIII in a simple case: if some fraction of the resolution elements all have the same ion density  $n_{\text{Ne VIII}}$ , and the rest contain no Ne VIII,  $1 / f_{c,v}$  is the fraction of the volume which contains Ne VIII ions.

We calculate  $f_{\text{fill}}$  in radial bins of size  $0.05 R_{\text{vir}}$  and show the smoothness as a function of (3D) distance to the halo center. We restrict this analysis to radial bins because the haloes are significantly denser in their centers than in their outskirts. A clumping factor measured over the whole halo would therefore not only be sensitive to how smoothly the Ne VIII is distributed, but also to how concentrated the ions are in the halo center. Measuring clumpiness in radial bins mitigates this issue, although this clumpiness measure is still sensitive to smooth, large-scale rotational asymmetries in ion density.

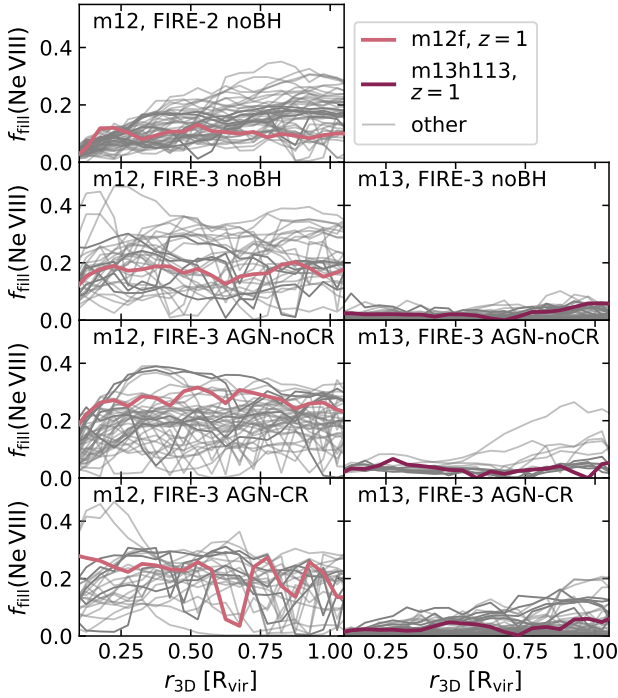


**Figure 3.** Filling fraction of the Ne VIII in the m12 and m13 haloes at redshifts 0.5, 0.6, 0.7, 0.8, 0.9, and 1.0 with different physics models (different panels). We calculate the filling fraction as the volume-weighted Ne VIII number density, divided by the Ne VIII-weighted Ne VIII number density (see eq. 1). Values lie between 0 and 1; higher values mean the distribution is smoother. The colored curves show the haloes from Figs. 1 and 2. The Ne VIII distribution in the m13 haloes is typically clumpier than that in m12 haloes.

Nevertheless, in conjunction with Figs. 1 and 2, it is clear that the Ne VIII in the m12 haloes is more smoothly distributed than in the m13 haloes. A similar plot to Fig. 3 showing the volume-weighted gas density clumping factor shows that the m13 CGM is not intrinsically clumpier than the m12 CGM, meaning that the differences here are a result of how well (or poorly) Ne VIII probes the smooth, virialized gas in the halo.

Finally, we note that there seem to be some differences between the physics models in the level of clumpiness in the halo: the FIRE-2 noBH model seems to produce somewhat clumpier haloes than the three FIRE-3 models, especially in the halo center. For the m13 haloes, the FIRE-3 noBH model might produce clumpier haloes than the other two models, but most FIRE-3 AGN-noCR and AGN-CR snapshots seem to contain haloes of a similar clumpiness to the noBH haloes. Any clumpiness differences between the FIRE-3 m13 models are therefore tentative. We further note that these differences might relate to spherical asymmetries as well as clumps. For the differences between the m12 and m13 haloes, Figs. 1 and 2 make clear that clumpiness is a major factor, but these do not show clear differences between physics models. A further look into the issue of azimuthal asymmetries vs. clumping is outside the scope of this work.

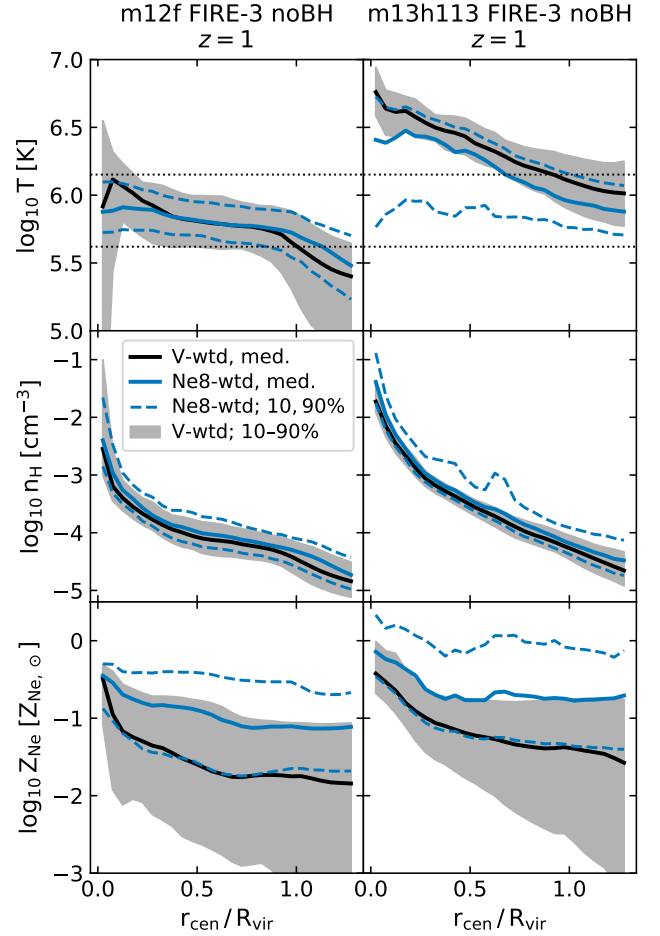


**Figure 4.** Temperature, density, and neon abundance profiles for an example m12 and m13 halo. We show the m12f FIRE-3 noBH halo and the m13h113 FIRE-3 noBH halo, both at  $z = 1$ . These haloes are shown in the second panel from the left in Fig. 1 and the left-hand panel in Fig. 2, respectively. Blue curves show Ne VIII-weighted medians (solid lines) and 10<sup>th</sup> and 90<sup>th</sup> percentiles of the Ne VIII-weighted distributions. Black curves and shading show the same percentiles of the volume-weighted distributions. The dotted, horizontal lines in the top panels show the range of temperatures where, for gas in collisional ionization equilibrium (CIE), the Ne VIII ion fraction is at least 0.1 times the maximum ion fraction in CIE.

### 3.2 Ne VIII and CGM properties

In Fig. 4, we explore the temperature, density and metallicity<sup>7</sup> of the Ne VIII in the CGM. We consider how Ne VIII traces the warm-hot CGM in these haloes, and whether the ionization of the neon is driven primarily by electron collisions (collisional ionization equilibrium, or CIE) or by photo-ionization (photo-ionization equilibrium or PIE).

In the top panels of Fig. 4, we show the volume- and Ne VIII-weighted temperature of an example m12 (left) and m13 (right) halo. We show the FIRE-3 noBH model for the m12f and m13h113 haloes at  $z = 1$ ; these haloes are also shown Figs. 1 and 2. The volume-weighted median and 10<sup>th</sup>–90<sup>th</sup> percentile temperatures (black) are shown in these top panels. The gas in the higher-mass m13 haloes, is, as expected, hotter than the gas in the m12 haloes. In the blue lines,

<sup>7</sup> We normalize the neon mass fraction by the Asplund et al. (2009) neon solar mass fraction  $10^{-2.90}$  here, following Ploekinger & Schaye (2020).

we show the same percentiles of the Ne VIII-weighted temperature distribution. In the m12 haloes, the Ne VIII traces roughly the same temperatures as the volume-filling gas phase. In the m13 haloes, Ne VIII traces the volume-filling phase as well, but it also traces cooler gas.

The horizontal dotted lines indicate why. For gas in collisional ionization equilibrium (CIE), these indicate the temperature range where the Ne VIII fraction is at least 0.1 times the maximum ionization fraction in CIE. In the m13 haloes, Ne VIII makes up a relatively small fraction of the neon in the volume-filling phase, especially in the halo center. Though there is less gas at temperatures where the Ne VIII fraction is high, what gas there is contains relatively many Ne VIII ions. In the m12 haloes, the volume-filling gas is at temperatures close to that where the Ne VIII fraction reaches its maximum, so this ion traces that volume-filling gas well.

In the middle panels of Fig. 4, we show the volume- and Ne VIII-weighted density percentiles in these same haloes. In the m12 haloes, the Ne VIII traces the density of the volume-filling gas quite well, with only a slight bias to higher densities. This bias towards high densities is stronger in the m13 haloes. This is in line with the clumpier Ne VIII distribution in m13 haloes relative to the m12 haloes.

Finally, we show the same distributions for metallicity (neon mass fraction) in the bottom panels of Fig. 4. Unsurprisingly, the Ne VIII preferentially traces neon-enriched gas. Though different haloes and physics models have different metallicity profiles, the median Ne VIII-weighted metallicity consistently lies roughly along the 90<sup>th</sup> percentile of the volume-weighted metallicity profile.

From these profiles, we can see that in both m12 and m13 haloes, gas within  $R_{\text{vir}}$  is typically at temperatures associated with CIE. However, some gas around  $R_{\text{vir}}$  in some m12 haloes is photo-ionized, and gas outside  $R_{\text{vir}}$  in m12 haloes is typically photo-ionized. Additionally, gas in m12 haloes, and in the outer regions of m13 haloes, may be at temperatures associated with CIE, but the gas density there is often low enough that the fraction of neon in the Ne VIII ionization state is affected by photo-ionization. In other words, much of the Ne VIII in m12 haloes, and in the outskirts of m13 haloes, is not clearly in photo-ionization equilibrium (PIE) or CIE, but instead ionized by both photons and electrons.

For more on the temperatures and densities of the CGM in these haloes, see Sultan et al. (in prep).

### 3.3 What determines the CGM Ne VIII content?

We have seen that Ne VIII broadly traces warm-hot gas in the CGM, and is an especially good tracer of the volume-filling gas in  $M_{\text{vir}} \sim 10^{12} M_{\odot}$  haloes. Now we explore which CGM properties determine the Ne VIII content of the haloes most strongly. We focus on the m12 haloes here, since we will later see that this is where most of the observational constraints are.

In the top left panel of Fig. 5, we show the average Ne VIII column densities in the haloes simulated with the different physics models. This illustrates the magnitude of the column density differences we want to explain. The clearest difference is between the FIRE-2 noBH model, and the three FIRE-3 models: the FIRE-2 model predicts higher Ne VIII column densities than the FIRE-3 models.

In the top right panel, we show histograms of the warm-hot ( $> 10^5$  K) CGM gas mass, normalized to the halo baryon budget, for our m12 sample. We find warm-hot CGM masses of roughly 0.1–0.3 times the halo baryon budget. The warm-hot CGM mass distributions for the different physics models are similar. We specifically consider the warm-hot gas, since we do not expect Ne VIII to be very sensitive to the cooler gas in the CGM (see e.g. Fig 4).

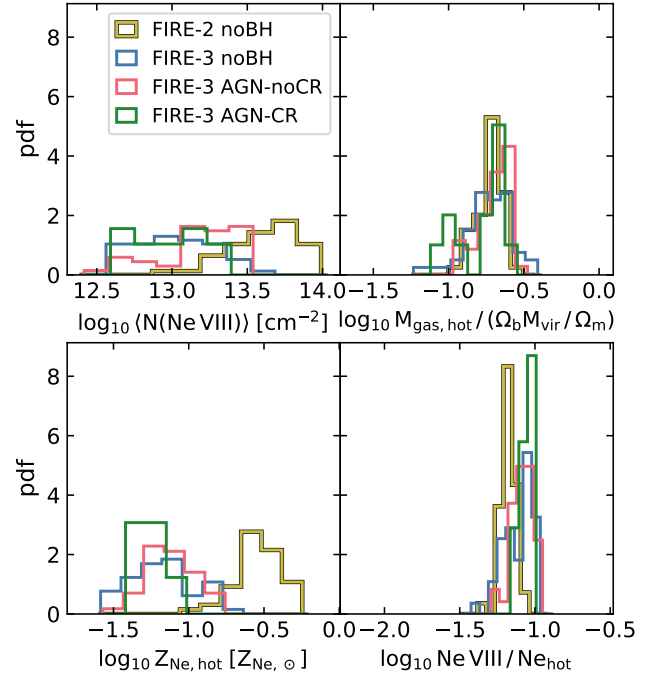


**Figure 5.** Histograms of various CGM properties determining the Ne VIII content of m12 haloes. Different colors show histograms for different physics models. For each physics model, the histograms show probability density functions calculated over each halo run with that physics model, at redshifts 0.5, 0.6, 0.7, 0.8, 0.9, and 1.0. The top left panel shows the mean CGM Ne VIII column density, calculated by dividing the number of Ne VIII ions between 0.1 and 1  $R_{\text{vir}}$  by  $\pi R_{\text{vir}}^2$ . As shown in Fig. 1, the FIRE-2 noBH column densities are higher than those of the FIRE-3 models. The top right panel shows the hot ( $> 10^5$  K) gas mass between 0.1 and 1  $R_{\text{vir}}$ , normalized to the halo mass and the cosmic baryon fraction. The bottom left panel shows the mass-weighted metallicity of the ( $> 10^5$  K) gas between 0.1 and 1  $R_{\text{vir}}$ . The FIRE-2 noBH model has a markedly higher metallicity than the FIRE-3 models, and the difference is large enough to explain the column density differences. Finally, in the bottom right panel, we show the Ne VIII ion mass between 0.1 and 1  $R_{\text{vir}}$ , divided by the  $T > 10^5$  K neon mass in that same radial range. Note that for the FIRE-3 AGN-CR model, we only have two haloes available.

The similar warm-hot CGM gas fractions are in line with the similar  $z \sim 0$  CGM mass fractions found by [Hafen et al. \(2019, fig. 2\)](#) in FIRE-2 noBH simulations, and found by Sultan et al. (in prep.) in FIRE-3 noBH/AGN-noCR m12 haloes.

In the bottom left panel of Fig. 5, we compare the (mass-weighted mean) metallicity of the warm-hot CGM ( $> 10^5$  K, 0.1–1  $R_{\text{vir}}$ ) in our different physics models. Here, we see clear differences: the FIRE-2 noBH simulations, with the highest Ne VIII column densities, also have clearly higher metallicities than the FIRE-3 models. The differences are of the right size to explain the column density differences.

Finally, in the bottom right panel of Fig. 5, we check the ratio of Ne VIII to neon in the warm-hot CGM. Note that we divide all Ne VIII at 0.1–1  $R_{\text{vir}}$  by the neon at 0.1–1  $R_{\text{vir}}$  and  $T > 10^5$  K. However, most Ne VIII is at temperatures  $> 10^5$  K. Here, we see a slightly lower Ne VIII fraction in the FIRE-2 noBH model, compared to the FIRE-3 models. The differences are, however, small compared to the metallicity and column density differences between the models.

We conclude that the Ne VIII column densities are higher in the

FIRE-2 simulations than in the FIRE-3 simulations due to the higher metallicity of the FIRE-2 noBH warm-hot CGM. We have checked that the neon abundance differences reflect the total metallicity differences between the models. The different models also include haloes with a similar  $M_{\text{vir}}$  distribution, except that the two FIRE-3 AGN-CR haloes are at the higher end of the  $M_{\text{vir}}$  distribution.

We speculate that the metallicity differences might share an origin with the lower stellar masses in the FIRE-3 noBH and AGN-noCR models compared to FIRE-2 noBH, and the even lower stellar masses for FIRE-3 AGN-CR. Lower stellar masses mean lower metal production, and therefore a lower halo metal budget. We have checked that the magnitudes of the warm-hot CGM metal content differences are in line with the central galaxy stellar mass differences. However, the total gas-phase metal contents of the haloes (0-1  $R_{\text{vir}}$ , all temperatures) do not reflect these stellar mass differences as nicely, so the effect is at least more complicated than a uniformly higher metallicity in the halo due to higher metal production in the FIRE-2 noBH model. In Appendix B, we show that FIRE-3 noBH haloes with higher halo masses, and stellar masses comparable to those of the FIRE-2 noBH haloes, still produce lower Ne VIII column densities than those FIRE-2 noBH haloes.

## 4 COMPARISON TO NE VIII OBSERVATIONS

### 4.1 How to compare observed and simulated haloes

#### 4.1.1 The CASBaH data

We compare our FIRE predictions for Ne VIII column densities to the observations of Burchett et al. (2019). Specifically, we use some of the quantities in their table 1. Briefly, their data combines a set of absorption spectra, which they searched for Ne VIII absorption, with the CASBaH (COS Absorption Survey of Baryon Harbors) galaxy catalogue (Prochaska et al. 2019). This catalogue includes galaxy spectroscopic redshifts, and galaxy stellar masses determined with spectral energy distribution (SED) fits and those redshifts.

These galaxies are matched to Ne VIII absorption systems<sup>8</sup> found along the sightline based on impact parameter ( $< 450$  pkpc) and velocity difference ( $< 500$  km s<sup>-1</sup>). They select the closest galaxy to the line of sight if there are different options.

For galaxies without corresponding absorbers, a  $3\sigma$  upper limit on the Ne VIII column density was determined. That means we can treat this as a survey where any sightline passing close enough to a galaxy was searched for absorption by that galaxy's halo. Therefore, medians and percentiles of the column densities around haloes at a given impact parameter are a good comparison for the measurements and upper limits in the data.

#### 4.1.2 The CUBS data

We also compare our Ne VIII column densities to the observations of Qu et al. (2023). Their analysis is part of the CUBS survey (Chen et al. 2020). Qu et al. (2023) searched for Ne VIII absorption at redshifts  $0.43 \lesssim z \lesssim 0.72$  in quasar spectra, and compiled a catalogue of galaxies close to their quasar sightlines. The CUBS and CASBaH quasar sightline samples do not overlap (Burchett et al. 2019; Chen et al. 2020), meaning the two datasets are independent of each other.

<sup>8</sup> Burchett et al. (2019) grouped individual absorbers into absorption systems if they were within  $\approx 600$  km s<sup>-1</sup> of each other. The redshift attributed to the absorption system is its central velocity.

Qu et al. (2023) determined their galaxy redshifts spectroscopically. Stellar masses were calculated based on three photometric bands. The relation Qu et al. (2023) used for this was fitted to a calibration sample of galaxies, with stellar masses derived from spectral energy distribution fits. Scatter in the fitted relation causes an estimated systematic error in the stellar masses of  $\approx 0.2$  dex. Qu et al. (2023) calculate halo masses  $M_{200c}$  from their stellar masses.

Galaxies were matched to absorbers in two steps. First, all galaxies within within  $3 R_{200c}$  of the sightline were selected. Galaxies were then grouped if they were within 1 Mpc and  $500$  km s<sup>-1</sup> of each other. Second, absorbers are matched to (groups of) galaxies if they have a velocity separation  $\leq 1000$  km s<sup>-1</sup>. For galaxies and groups without measured column densities,  $2\sigma$  upper limits on the Ne VIII column densities were determined. Within groups, a single galaxy is selected as the absorber counterpart. Based on correlations with O VI absorption, Qu et al. (2023) chose the galaxy with the smallest impact parameter in units of  $R_{200c}$  as this counterpart.

As with the Burchett et al. (2019) measurements, it is therefore reasonable to compare the measurements and upper limits of Qu et al. (2023) to medians and other percentiles of the Ne VIII column density predicted by FIRE.

#### 4.1.3 Halo masses

Our goal is to compare the FIRE CGM to the CGM observations of Burchett et al. (2019) and Qu et al. (2023). The Burchett et al. (2019) observations are of Ne VIII CGM absorbers around isolated galaxies with stellar masses  $\sim 10^9$ – $10^{11} M_{\odot}$ . For CGM comparisons to observations, matching the halo masses is important, because the halo mass determines the CGM baryon budget, extent, and virial temperature, i.e., three important factors determining the ion content of the warm/hot phase. Burchett et al. (2019) measured the stellar masses of their galaxies, and used a modified version (Burchett et al. 2016) of a function fit to abundance matching simulations (Moster et al. 2013) to obtain halo masses based on these stellar masses.

Burchett et al. (2019) do not, however, report errors on the halo masses. Since there is scatter in the stellar-mass-halo-mass relation, these could be quite large. Therefore, we used a UniverseMachine stellar and halo mass catalog<sup>9</sup> (Behroozi et al. 2019) to reconstruct the stellar-mass-halo-mass relation and look into some sources of errors.

Specifically, we used the catalogues based on the Small Multi-Dark-Planck (SMDPL) dark-matter-only simulation (Klypin et al. 2016; Rodríguez-Puebla et al. 2016), which has a volume of  $(0.4 \text{ Gpc} / h)^3$ . Behroozi et al. (2019) analysed these using the ROCKSTAR halo finder (Behroozi et al. 2013a) and CONSISTENT TREES Behroozi et al. (2013b) merger trees. We only used UniverseMachine galaxies flagged as centrals for this analysis.

From this catalogue, we estimate the true halo mass probability distribution given an observed galaxy stellar mass and redshift. We do this by finding the distribution of halo masses in the catalogue for a given stellar mass, and then combine that with the probabilities of different true stellar masses from the observations.

This different method makes a difference for the most likely halo masses inferred, which is quite large for central galaxies with stellar masses  $\geq 10^{10.5} M_{\odot}$ . Accounting for scatter in the stellar-mass-halo-mass relation also leads to larger uncertainty estimates, again mostly at  $M_{\star} \geq 10^{10.5} M_{\odot}$ . We give a more detailed explanation of our

<sup>9</sup> [https://halos.as.arizona.edu/UniverseMachine/DR1/SMDPL\\_SFR/](https://halos.as.arizona.edu/UniverseMachine/DR1/SMDPL_SFR/), accessed 2023-06-15



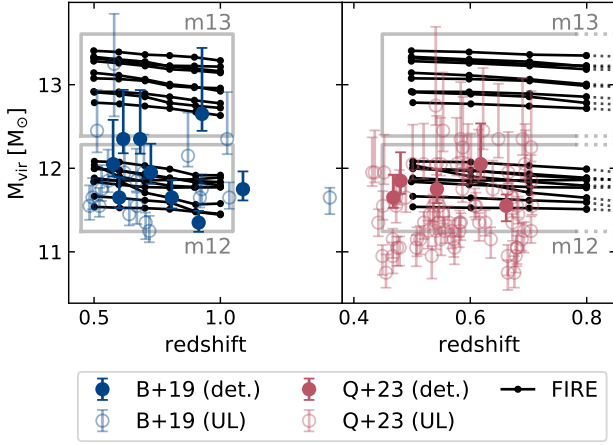


**Figure 6.** Halo masses (Bryan & Norman 1998, definition) and redshifts for the simulated halos (black lines), compared to the distribution of halo masses and redshifts of the galaxies Burchett et al. (2019) (left) and Qu et al. (2023) (right) found within 450 pkpc of their quasar sightlines. If a halo was simulated with different physics models, we only show its mass as a function of redshift for one model. We calculate the observed galaxy halo masses as described in §4.1. Filled points indicate systems where the observers measured the Ne VIII column density, while open points are haloes where they set an upper limit instead. The points show the halo mass with the highest probability, and error bars show the  $1\sigma$  uncertainties. The boxes indicate the ranges of mass and redshift where we consider data points good matches to the m12 and m13 halo samples.

method, and our recommendations for how to estimate these halo masses, in Appendix A.

Qu et al. (2023) did determine their halo masses using a stellar-mass-halo-mass relation from Behroozi et al. (2019). However, they use an overdensity of 200 relative to the critical density to define haloes, where we use the Bryan & Norman (1998) density definition, and they do not report errors on their halo masses. We therefore apply the same method to the CUBS stellar masses to calculate the most likely halo mass, and its errors, as we applied to the CASBaH data.

## 4.2 Column density profiles

In Fig. 6, we show the masses and redshifts of the haloes in our simulated sample, and the observed samples of Burchett et al. (2019) and Qu et al. (2023). The black lines indicate the masses and redshifts of different haloes. If a halo was simulated with different physics models, we only show the masses and redshifts for one of them. This is for legibility, and is reasonable because the halo masses differ little between these simulations with different physics models. For the observed data points, we show the most likely halo masses with points; these are maximums of the curves in Fig. A2. The  $1\sigma$  uncertainty ranges show the log halo mass range enclosing a probability of 68%.

We only show data points with impact parameters  $< 450$  pkpc in Fig. 6. For the CASBaH data, this matched their own galaxy selection, but this excludes some of the CUBS upper limits, especially at high halo masses. We focus on these impact parameters because, for the m12 haloes, this 450 pkpc is  $\approx 2\text{--}3 R_{\text{vir}}$ , which is towards the edge of the zoom-in region of the simulations. For the m13 haloes, larger impact parameters might be acceptable given the volume of the zoom

region, but the CUBS upper limits there are not very constraining, so we prefer to focus on the impact parameters where Ne VIII was detected.

The gray boxes are drawn at the minimum and maximum halo mass and redshift in the m12 and m13 samples, with a redshift margin of 0.05, and a log halo mass margin of 0.2. An observed galaxy is considered a good match to the m12 or m13 FIRE sample if its best-estimate halo mass and redshift fall within the solid box. In Figs. 7 and 8, these haloes are shown with black markers. We will also compare FIRE predictions to data points in larger sections of this plot, using larger margins of 0.1 in redshift and 0.4 in log halo mass. We consider data points in these larger regions to be plausible matches. In Figs. 7 and 8, these haloes are shown with grey markers. These margins for the most likely halo masses seem to be fairly consistent with whether the halo mass uncertainties include the simulated ranges.

In Figs. 7 and 8, we compare the m12 and m13 halo column densities in the FIRE-3 simulations to the measurements of Burchett et al. (2019) and Qu et al. (2023). In the FIRE-3 m12 haloes, the observed column densities are consistently above the measured values. The FIRE-2 noBH model can reproduce some of the measurements, although it does not produce the highest observed column densities often enough to explain these detections. We note that for the FIRE-2 noBH model, a higher median column density in the halo center would likely be in tension with the Qu et al. (2023) upper limits. It is therefore possible that matching observations would instead require a larger column density scatter, or column densities which decline more gently with impact parameter.

The FIRE-3 m13 haloes match two plausibly matched Burchett et al. (2019) column densities, but all models underpredict the column density of the one measurement which clearly matches the m13 halo mass range. We note that this is also the highest measured value in the Burchett et al. (2019) sample. The discrepancies seem to be largest for the AGN-CR model, which has lower central Ne VIII column densities than the other m13 models.

## 5 ANALYTICAL MODELING

Some of the Burchett et al. (2019) and Qu et al. (2023) column densities are higher than predicted in any of our FIRE models. Some of these, such as the  $\approx 10^{14} \text{ cm}^{-2}$  absorption system at an impact parameter of  $\approx 400$  pkpc, might be outliers: this data point lies above many upper limits at smaller impact parameters. However, our models might also simply be wrong.

To check whether the observed column densities are achievable within our current, broad understanding of the CGM, we predict column densities using a simple analytical model. The goals here are (1) to see how we expect the column densities to depend on the halo mass, size, and temperature, and (2) to check whether the high Burchett et al. (2019) and Qu et al. (2023) column densities can be explained in theory.

The first goal mainly matters because we sample haloes in two specific mass ranges, but some of the halo masses in the observational data may lie below or between these ranges. Therefore, it is useful to know if we should expect some of these haloes outside the mass ranges we probe with FIRE to produce meaningfully different Ne VIII column densities from those we do have. With the second goal, we explore whether the high column densities signal issues with FIRE specifically, or theoretical CGM models more broadly.

In our analytical model, we assume the various thermodynamical properties of the halo gas are in a steady state, and are power law

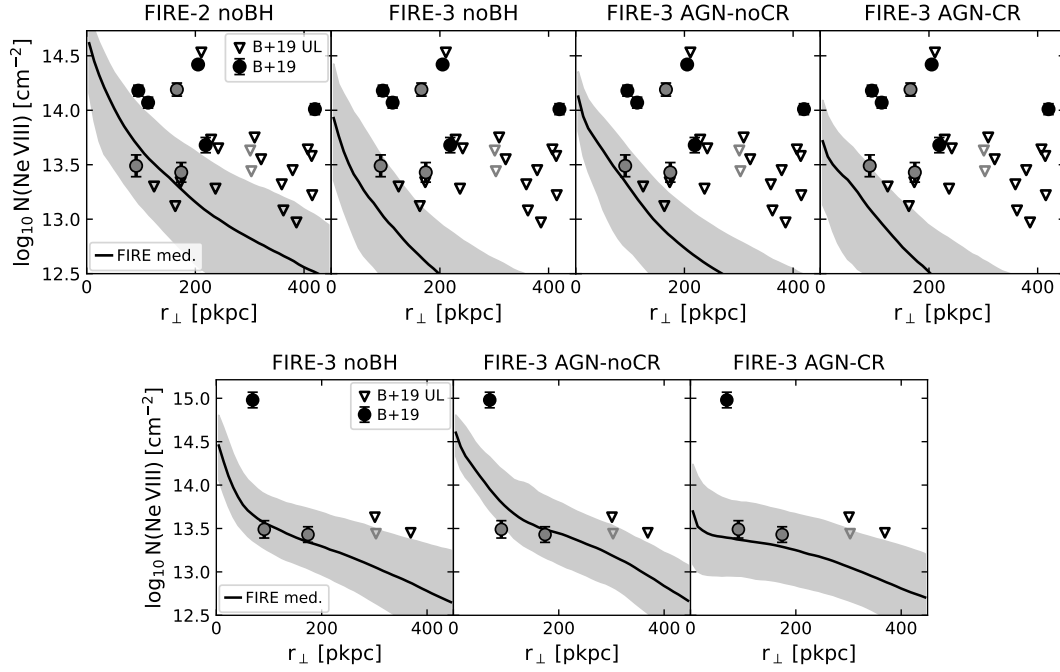


**Figure 7.** Ne VIII column densities predicted from our simulations, compared to the values (points with  $1\sigma$  error bars) and upper limits ( $3\sigma$ , open triangles) found by [Burchett et al. \(2019\)](#). The black points show observed galaxies which match the m12 (top panels) and m13 (bottom panels) halo mass and redshift range well, and gray points show plausible matches (see text for the precise selections). For the simulation data, solid lines show median column densities as a function of impact parameter, while the shaded region shows the percentile 10–90 range of the column density at a given impact parameter. Different panels show different physics models, indicated above each panel. The m12 FIRE-2 noBH model matches some of the observed column densities, but does not match the highest measured values, while all three m12 FIRE-3 models predict column densities below most of the measurements. The m13 haloes match two of the observed column densities, but underpredict the largest measured value.

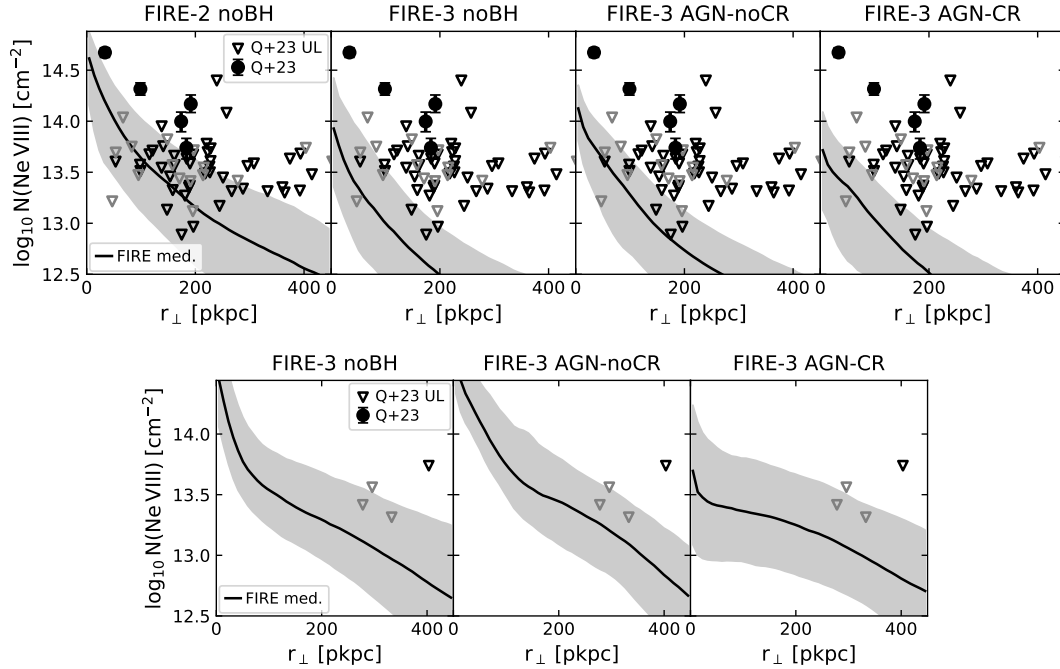


**Figure 8.** As. Fig. 7, but comparing the m12 (top row) and m13 (bottom row) halos to the [Qu et al. \(2023\)](#) observations. The error bars on their measurements and their upper limits are both  $2\sigma$ . Again, the FIRE-2 noBH m12 haloes match one of the measurements, but all physics models underpredict the highest measured column densities. The m13 haloes are consistent with the measured upper limits.

functions of distance to the halo center. We describe the gravitational potential as

$$v_c \propto r^m, \quad (2)$$

where  $v_c$  is the circular velocity,  $r$  is the distance to the halo center, and  $m$  is an exponent to be determined. We additionally try a few different values of the entropy profile logarithmic slope

$$l \equiv \frac{d \ln K}{d \ln r}, \quad (3)$$

where  $K$  is the entropy  $K = kTn^{-\frac{2}{3}}$ ,  $k$  is the Boltzmann constant, and  $n$  is the gas particle number density.

This results in a power-law temperature profile  $T \propto r^{2m}$ , with a normalization depending on  $l$ ,  $m$ , and  $v_c$  at the virial radius. We calculate this simply as  $v_c(R_{\text{vir}}) = \sqrt{\frac{GM_{\text{vir}}}{R_{\text{vir}}}}$ . The density profile is given by  $n_H \propto r^{-\frac{3}{2}l+3m}$ , and we set the normalization by requiring that the mass of this CGM gas is the cosmic baryon fraction of the halo mass  $M_{\text{vir}}$  (within  $R_{\text{vir}}$ ). We derive these equations in appendix C.

We realize that assuming the warm/hot CGM contains the cosmic baryon fraction of the halo in mass is a very optimistic assumption, as it leaves no ‘space’ for central and satellite galaxies or a cool CGM phase. However, avoiding assumptions on those other mass fractions does keep the model simple, and we want to explore an extreme model here to assess the consistency of the high column density measurements with our current understanding of the CGM in a broad sense.

We will also explore lower values of  $f_{\text{CGM}} = M_{\text{CGM}} / (\Omega_b M_{\text{vir}} / \Omega_m)$ , where  $M_{\text{CGM}}$  is the (warm/hot) CGM mass. Rescaling the density profile by this single value will, however, unphysically lower the gas density outside the halo for lower CGM gas fractions. In practice, we would expect a lower CGM gas fraction to correspond to a shallower density profile, with gas being pushed out or retained beyond  $R_{\text{vir}}$ , raising the density there.

In calculating the column densities for these profiles, we further assume a metallicity of  $0.3 Z_\odot$ <sup>10</sup>, and a hydrogen mass fraction of 0.752 in the density profile normalization. We calculate ion fractions using the Ploekinger & Schaye (2020) ionization tables, in the same way as for the FIRE predictions.

Next, we need to decide on a circular velocity profile slope  $m$ . We base these choices on the  $v_c$  slopes in NFW halo mass profiles (Navarro et al. 1997). In these profiles, the circular velocity profile slope  $\frac{d \log v_c}{d \log r}$  depends on  $\frac{r}{r_s}$ , where  $r_s$  is a scale radius. We roughly estimate the relation between  $r_s$  and  $R_{\text{vir}}$  using table 3 of Dutton & Macciò (2014); this yields concentrations  $R_{\text{vir}}/r_s \approx 6-9$  for haloes with  $M_{\text{vir}} = 10^{11.5}-10^{13.5} M_\odot$  around redshifts 0.5 and 1, decreasing with halo mass. This yields slopes  $\frac{d \log v_c}{d \log r} \approx -0.2$  to 0.25 in the radial range  $0.1-1 R_{\text{vir}}$ . The slopes decrease (become more negative) with halo center distance and increase (become more positive) with halo mass. We choose a circular velocity slope  $m = -0.1$ , which is reasonable for the large radii (in virial radius units) where many of the measurements most likely lie.

For the entropy slopes, we show a range of plausible values. Zhu et al. (2021) find outer halo entropy slopes  $\approx 1.2$  from an observational group/cluster sample. Babyk et al. (2018) study entropy profiles in haloes over a range of masses, using observations around early-type galaxies and clusters. At small radii, their findings are consistent with a slope of  $\frac{2}{3}$ , and at larger radii with 1.1. An entropy

slope of zero can occur in e.g., cluster centers, and can arise due to convective instability.

We note that not all entropy and circular velocity profile combinations are possible. If both slopes are zero, there is no pressure gradient, the assumption of hydrostatic equilibrium becomes meaningless, and the temperature profile normalization is not constrained. If  $l$  is too large and/or  $m$  is too negative, the density slope becomes too steep and the mass integral within the virial radius diverges.

We show these model Ne VIII profiles in Fig. 9, alongside the observations. We note that the upper limits are  $2\sigma$  for Qu et al. (2023, red) and  $3\sigma$  for Burchett et al. (2019, blue). The high measured column densities can be achieved in a power-law CGM model, containing the cosmic baryon fraction of the halo mass in the warm-hot CGM phase, and with a uniform metallicity of  $0.3 Z_\odot$ . Though this is an extreme model, it does not conflict with our basic sense of what the CGM could look like. We do note that the validity of these models beyond  $R_{\text{vir}}$  is uncertain.

We also note that the haloes producing the highest column densities are at the high end of the  $m12$  mass range (see Fig. 6), meaning these haloes are represented in our simulation sample.

In Fig. 10 we further explore these power law models in relation to the measured column densities. We choose the halo mass from Fig. 9 consistent with the most data points,  $M_{\text{vir}} = 10^{12.2} M_\odot$ , and explore whether the data is consistent with less extreme CGM mass fractions than the cosmic baryon fraction of Fig. 9.

We see that some data points are indeed consistent with lower CGM masses  $\sim 0.3 \Omega_b / \Omega_m M_{\text{vir}}$ , although we note that we are still assuming a constant metallicity of 0.3 times solar throughout the halo. Metallicity and CGM mass are not precisely degenerate in this column density model, as the CGM mass (along with the chosen entropy and circular velocity slopes) determines the density profile. Lower densities can affect the ionization balance if they are low enough for photo-ionization to become important. In practice, a model with CGM mass  $0.3 \Omega_b / \Omega_m M_{\text{vir}}$  and solar metallicity looks similar to the model with CGM mass  $\Omega_b / \Omega_m M_{\text{vir}}$  and 0.3 times solar metallicity shown in blue in Fig. 10. The largest differences are furthest from the halo center and with the steepest entropy slope.

However, some data points can only be explained with this power-law model of the volume-filling phase if the CGM mass and metallicity are high, and if the entropy slope is high. (Note that in a cooling flow model, choosing a particular circular velocity slope can also lead to a match.) This implies that these high measured column densities might be probing very gas-rich haloes, or perhaps particularly dense or metal-enriched warm/hot gas within a halo. We do expect Ne VIII to broadly trace the volume-filling gas in a halo of the mass in Fig. 10, but Figs. 1 and 3 show that some denser-than-average Ne VIII can exist in these haloes.

The metallicities and CGM warm-hot gas content in the FIRE haloes (Fig. 5) paint a similar picture to our analytical model: the FIRE-2 noBH model has halo metallicities  $\sim 0.3$  times solar, and  $f_{\text{CGM}}$  parameters in the  $\approx 0.1-0.3$  range. As the analytical models would suggest, some haloes match many observations, but under-shoot the largest values, and some haloes have column densities which only match the lower measured Ne VIII column densities. The other models, with similar  $f_{\text{CGM}}$ , but metallicities around and below  $\approx 0.1$  times solar, are consistent with the lower measured column densities, but lie below most observed values.

<sup>10</sup> We use the Asplund et al. (2009) neon solar abundance  $\frac{n(\text{Ne})}{n(\text{H})} = 8.51 \times 10^{-5}$  here, following Ploekinger & Schaye (2020).

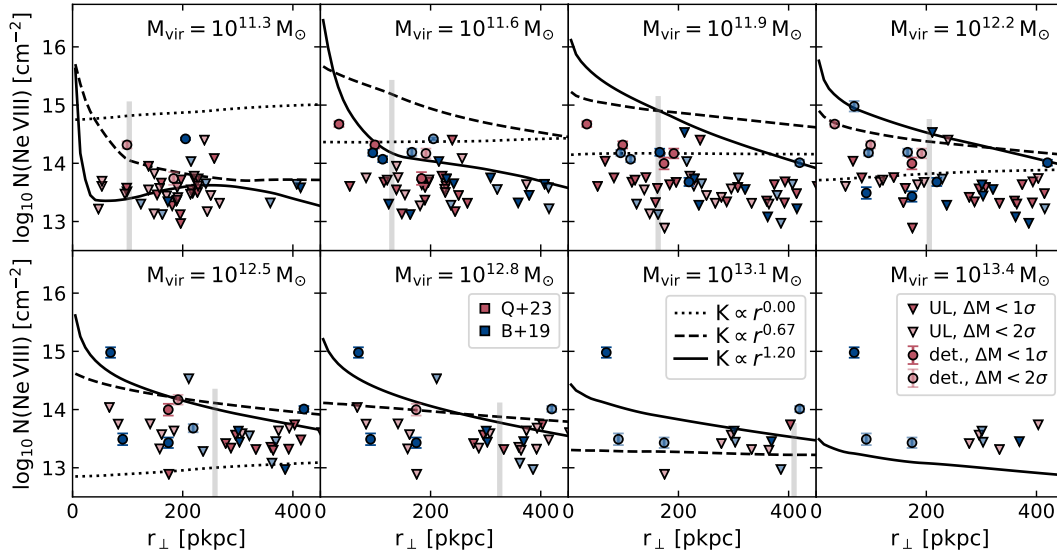


**Figure 9.** Ne VIII column density as a function of impact parameter for some power law CGM models with a warm/hot CGM mass budget  $f_{\text{CGM}} = 1$  and a uniform metallicity of  $0.3 Z_{\odot}$ . Different logarithmic entropy slopes are shown in different line styles. We use a circular velocity slope  $m = -0.1$ . Each panel shows one halo mass, indicated in the upper right of the panel. We show how the measurements (points with error bars) and upper limits (downward-facing triangles) of Burchett et al. (2019, blue) and Qu et al. (2023, red) compare to these models. The brighter measurement and upper limit points have halo masses within  $1\sigma$  of the halo mass shown in the panel, while points with lighter colors have halo masses between 1 and  $2\sigma$  from the model halo masses. Vertical gray lines indicate the virial radius; for  $M_{\text{vir}} = 10^{13.4} M_{\odot}$ , this radius is outside the plotted range. All measurements seem achievable in some variation of a power law model with a very high gas fraction and a uniform metallicity of  $Z = 0.3 Z_{\odot}$ . However, for the highest column density measurement, this is only possible here if the halo mass is at the low end of the possible halo mass range, and only for the model with entropy slope  $l = 1.2$ .

## 6 DISCUSSION

We have compared various FIRE simulations of  $\sim 10^{12} M_{\odot}$  (m12) and  $\sim 10^{13} M_{\odot}$  (m13) haloes at  $z = 0.5-1.0$  to observations of CGM Ne VIII absorbers by Burchett et al. (2019) and Qu et al. (2023). For the m13 haloes, the data is limited, but the FIRE predictions are mostly consistent with the data we do have. For the m12 haloes, we find that the FIRE-2 noBH model produces higher Ne VIII column densities in the CGM than the three FIRE-3 models we examine, including one that similarly has no AGN feedback. This is largely due to the higher CGM metallicity in the FIRE-2 haloes. The FIRE predictions for the m12 Ne VIII column densities match some of the data, but underpredict the higher measured column densities.

Within the FIRE samples we analysed, the m12 FIRE-2 noBH model seems to reproduce the Ne VIII observations better than the FIRE-3 models. However, as we discuss in Appendix B, differences in central galaxy stellar masses seem to contribute to these differences. Hopkins et al. (2018b) found that the FIRE-2 galaxy stellar masses were somewhat high for their halo masses. Byrne et al. (in prep.) find that for the m12 haloes, the FIRE-3 noBH and AGN-noCR models reasonably match the  $z \approx 0$  stellar-mass-halo-mass relation. Generally, the FIRE-3 m12 haloes have lower stellar masses than FIRE-2 haloes with the same halo mass (Hopkins et al. 2023). In the m13 haloes, the FIRE-3 noBH model produces galaxies which are too massive and compact. However, we generally caution that which FIRE-3 model ‘does best’ depends on the galaxy property being considered (Byrne et al. in prep.).

The small sample sizes (in both FIRE haloes and measured absorbers) do add uncertainty to these (mis)matches. The large uncertainties in some of the observed galaxies’ halo masses and the lack of ‘contamination’ from nearby haloes and/or IGM in the FIRE zoom regions also introduce some systematic uncertainties into the comparisons. In Appendix B, we show that FIRE-3 noBH haloes with

higher masses produce higher Ne VIII column densities, while the halo mass range is consistent with essentially the same observations. The uncertainty means that which model matches the observations best is also somewhat uncertain.

### 6.1 Why are the FIRE column densities low?

In §5, we saw that analytical CGM models with high warm/hot CGM gas fractions can match the highest measured data points, which our FIRE simulation samples underpredict. Analytical models with a given warm/hot CGM gas fraction and metallicity also seem to broadly compare to observations similarly to FIRE models which produce similar gas fractions and metallicities.

We note that in the FIRE ecosystem, the differences between Ne VIII column densities predicted by different models are largely driven by metallicity differences. However, different simulations which produce realistic  $z \approx 0$  galaxy populations can also have meaningfully different CGM gas fractions at  $M_{\text{vir}} \sim 10^{12} M_{\odot}$  (Davies et al. 2020), so both the warm/hot gas fractions and the metallicities could underlie the differences between our simulations and the observations of Burchett et al. (2019) and Qu et al. (2023).

We also note that there are uncertainties on the observational side. Aside from the uncertainty in halo masses, the Ne VIII 770, 780 Å doublet falls in a crowded part of the spectrum (e.g. Burchett et al. 2019, fig. 6). This makes it more difficult to measure the equivalent width and line width of an absorber, and even to identify the doublet. This might explain some of the differences between the Qu et al. (2023) and Burchett et al. (2019) data: within 450 pkpc of galaxies, Burchett et al. (2019) measure column densities  $\geq 10^{14} \text{ cm}^{-2}$  in 6 out of 28 sightlines, while Qu et al. (2023) measure absorption of this strength in 3 out of 65 sightlines. (We excluded sightlines with column density upper limits  $\geq 10^{14} \text{ cm}^{-2}$  from our counts.) These



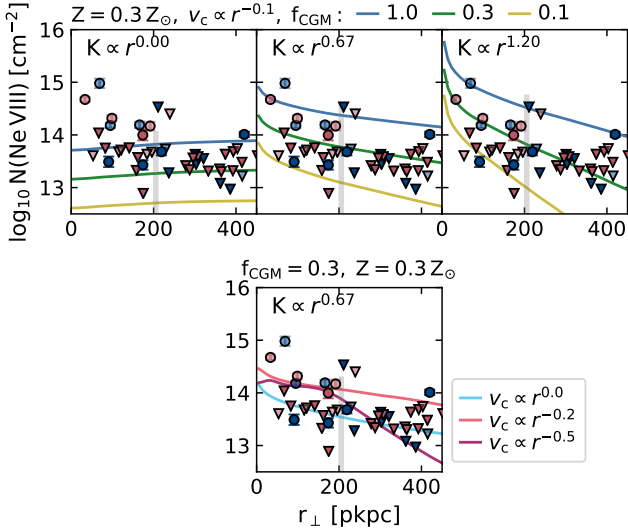


**Figure 10.** *Top row:* A comparison of analytical models with different CGM baryon fractions  $f_{\text{CGM}} = M_{\text{CGM}} / (\Omega_b M_{\text{vir}} / \Omega_m)$ , where  $M_{\text{CGM}}$  is the (warm/hot) CGM mass. We show power law models with different entropy slopes for a halo with  $M_{\text{vir}} = 10^{12.2} M_{\odot}$  and a metallicity of  $0.3 Z_{\odot}$  at redshift  $z = 0.75$ . Different entropy slopes are shown in different panels and slope values are given in the upper left of each plot. Model column densities are shown for CGM masses of 1.0, 0.3, and 0.1 times the cosmic baryon fraction of the halo mass. The measurements are shown in the same way as Fig. 9, and vertical, gray lines indicate the virial radius. While some data points are consistent with CGM masses only 0.1 times the universal baryon fraction in a halo, other measurements are only consistent with our power law model with a high baryon fraction and metallicity, and a high entropy slope. *Bottom row:* for one entropy slope, we show the effect of varying the circular velocity profile slope. The differences between the profiles are generally smaller than those over the plausible range of entropy slopes, but the effects are not negligible.

are small numbers, impacted by e.g., a Qu et al. (2023) absorber with a Ne VIII column density barely below  $10^{14} \text{ cm}^{-2}$ . However, the incidence of high column density CGM absorbers is clearly higher in the Burchett et al. (2019) data.

Finally, we note that the highest observed column density we compare to is  $\approx 10^{15} \text{ cm}^{-2}$ , measured by Burchett et al. (2019) and most consistent with an m13 host halo. Tripp et al. (2011) had previously measured this absorption system; it consists of many absorption components, some of which have large velocity offsets from the host galaxy or group. Tripp et al. (2011) concluded that Ne VIII was tracing an outflow in this system. In principle, FIRE haloes could include outflows. However, if this is a fairly rare system (likely to be detected due to its high column density), it might be reasonable that our set of haloes did not capture an outflow event like this, and its corresponding high column density.

## 6.2 How do other simulations fare?

Here, we consider whether other simulations and models can produce Ne VIII column densities that match these observations. Ji et al. (2020) had previously compared FIRE-2 simulations to the Burchett et al. (2019) data, focusing on differences between a model with cosmic rays and one without them. They find the model without cosmic rays agrees well with the Ne VIII observations, although their CR model reasonably matches Ne VIII as well, and compares better to

observations of some other ion column densities. We find that our FIRE-2 noBH model matches some of that data, but underpredicts the higher measurements. We note that the comparisons are somewhat different. For example, Ji et al. (2020) use a single halo simulated with a different FIRE-2 physics model, assume a different UV/X-ray background, compare data in virial radius units, and show the mean column density while we plot the median.

Wijers et al. (2020) discuss Ne VIII column densities around haloes of different masses in the EAGLE simulations (Schaye et al. 2015; Crain et al. 2015; The EAGLE team 2017). The analysis in this paper is focused on  $z = 0.1$  (the other ions they study are accessible there), but in fig. C1, they show Ne VIII column densities at  $z = 0.5$ . This is only the lower end of the Burchett et al. (2019) observational redshift range, but in FIRE, we have not found a clear redshift evolution over the  $z = 1.0$ – $0.5$  range, and in EAGLE, the difference between redshifts 0 and 0.5 is small. Comparing to  $z = 0.5$  is therefore reasonable.

For the Wijers et al. (2020)  $M_{200c} = 10^{12.0}$ – $10^{12.5} M_{\odot}$  halo mass range<sup>11</sup>, the median column density does not depend very strongly on impact parameter, decreasing from  $\approx 10^{13.8}$  to  $\approx 10^{13.4} \text{ cm}^{-2}$  from 0.1–1  $R_{200c}$ . Haloes of  $M_{200c} = 10^{12.5}$ – $10^{13.0} M_{\odot}$  have similar column densities within their virial radius, and  $M_{200c} = 10^{11.5}$ – $10^{12.0} M_{\odot}$  haloes have  $\approx 0.4$  dex lower median column densities. The 90<sup>th</sup> percentile of column densities is at most  $\approx 10^{14.3} \text{ cm}^{-2}$ , at the center of the halo. The EAGLE column densities decrease quite rapidly beyond the virial radius.

In Fig. 9, we show the observed column densities consistent with different halo masses (indicated in the top right of each panel). The  $M_{200c} = 10^{12.0}$ – $10^{12.5} M_{\odot}$  EAGLE column densities seem to be reasonably consistent with some of the observations, but fall below most measured values, and the  $M_{200c} = 10^{11.5}$ – $10^{12.0} M_{\odot}$  Ne VIII EAGLE column densities are clearly too low. A notable difference between the simulations is that the EAGLE profiles are flatter than the FIRE profiles, including near the halo center, where the difference between zoom and large volume simulations should not matter (Wijers et al. 2020, fig. 8).

Liang et al. (2016) predict Ne VIII column densities from zoom-in simulations of a  $\sim 10^{12} M_{\odot}$  halo using the RAMSES code, comparing different feedback prescriptions. The Ne VIII column densities are  $\lesssim 10^{14} \text{ cm}^{-2}$  for the two models shown in their fig. 15, underpredicting the Burchett et al. (2019) and Qu et al. (2023) measurements for that halo mass. In comparisons of other CGM absorption lines to data, they conclude that models which produce realistic galaxies do not necessarily predict a realistic CGM.

Ford et al. (2013) predict Ne VIII column densities from a hydrodynamical simulation in a cosmological volume. This model produces reasonable  $\lesssim L_*$  galaxy properties, including the redshift 0 stellar mass function. They show median column densities at impact parameters of 10, 100, and 1000 pkpc, for haloes of  $10^{11}$ ,  $10^{12}$ , and  $10^{13} M_{\odot}$ . The column densities do not exceed  $\approx 10^{13} \text{ cm}^{-2}$  across these impact parameter and halo mass ranges, well below the measured values.

## 6.3 How do other analytical models fare?

A number of groups have predicted Ne VIII column densities from analytical models. For example, Faerman et al. (2022) combine CGM gas masses for  $10^{12} M_{\odot}$  haloes from the Santa Cruz semi-analytical

<sup>11</sup>  $M_{200c}$  is the mass in a sphere with a mean density 200 times the critical density at the halo redshift.

model (SAM) with an analytical model for CGM density, metallicity, etc. profiles. They predict column densities as seen from inside a galaxy (as would be measured for the Milky Way halo). They predict column densities of  $0.4\text{--}2 \times 10^{14} \text{ cm}^{-2}$ , depending on the halo CGM mass fraction. This would translate to column densities of  $10^{13.9}\text{--}10^{14.6} \text{ cm}^{-2}$  in sightlines through the halo center, increasing with gas fraction. Those values are plausibly consistent with the [Burchett et al. \(2019\)](#) and [Qu et al. \(2023\)](#) measurements, although most measurements consistent with this halo mass are at impact parameters  $\gtrsim 0.5 R_{\text{vir}}$ .

[Voit \(2019\)](#) predicts Ne VIII column densities at an impact parameter of 50 pkpc, as a function of halo mass, for different variations of a precipitation-limited CGM model. Depending on the exact model variation, these column densities reach  $\approx 10^{14}\text{--}10^{14.5} \text{ cm}^{-2}$  in haloes with  $M_{200c} \approx 1\text{--}2 \times 10^{12} M_{\odot}$ , with lower column densities at lower halo masses. These predictions seem roughly consistent with the observations at  $\approx 10^{12} M_{\odot}$ , though we note they assume the CGM at these masses has solar metallicity.

[Qu & Bregman \(2018\)](#) compare their analytical CGM model predictions to a different set of Ne VIII observations and find agreement. They predict column densities  $\sim 10^{14} \text{ cm}^{-2}$  for haloes with a mass  $\sim 10^{12} M_{\odot}$ , and column densities up to  $\approx 2 \times 10^{14} \text{ cm}^{-2}$  outside 0.3 virial radii in the different variations of their model. This is roughly the range of the [Burchett et al. \(2019\)](#) observations.

Although a number of these models predict column densities around  $\sim 10^{12} M_{\odot}$  haloes which are similar to observed values, we note that the  $\approx 10^{15} \text{ cm}^{-2}$  absorption system is not within any of the predicted ranges. The analytical models do not predict column densities outside the virial radius, but the  $\approx 10^{14} \text{ cm}^{-2}$  absorption system at an impact parameter of  $\approx 400$  pkpc is above the range predicted by all the hydrodynamical simulations we discussed here.

We also note that hydrodynamical simulations, which self-consistently predict galaxy and CGM properties, seem to struggle to predict the higher measured Ne VIII column densities, despite producing realistic galaxies. On the other hand, only the most extreme measurements are outside the range of the (semi)-analytical models. These observations therefore do not challenge our basic understanding of how much mass the CGM may contain, and which temperatures and metallicities are plausible. However, self-consistently producing both realistic galaxies and CGM seems to be more difficult. This points to a challenge in modeling galaxy formation and feedback, and highlights the value of CGM observations in understanding these processes.

## 7 CONCLUSIONS

We have analysed a set of FIRE-2 and FIRE-3 simulations run with different physics models to predict halo Ne VIII column densities from each. Specifically, we considered haloes with  $M_{\text{vir}} \sim 10^{12}$  and  $\sim 10^{13} M_{\odot}$ . We compared these predictions to the circumgalactic Ne VIII column densities measured by [Burchett et al. \(2019\)](#) and [Qu et al. \(2023\)](#). Our main conclusions are summarized below.

- At  $z = 0.5\text{--}1.0$ , in  $M_{\text{vir}} \sim 10^{12} M_{\odot}$  haloes, Ne VIII traces the relatively smooth, volume-filling phase of the CGM (Figs. 1 and 3). On the other hand, at  $M_{\text{vir}} \sim 10^{13} M_{\odot}$ , where the volume-filling phase is typically hotter than optimal for Ne VIII, this ion has a clumpier distribution (Figs. 2 and 3).
- In our  $M_{\text{vir}} \sim 10^{12} M_{\odot}$  haloes, Ne VIII is mostly at temperatures consistent with collisional ionization, although its density is often low enough that the ion fraction is affected by photo-ionization. Around and beyond  $R_{\text{vir}}$ , gas may also be photo-ionized. In  $M_{\text{vir}} \sim 10^{13} M_{\odot}$

haloes, gas is mostly collisionally ionized, with photo-ionization affecting ion fractions around and beyond  $R_{\text{vir}}$  (Fig. 4).

- The FIRE-2 noBH model tends to produce higher CGM Ne VIII column densities than the FIRE-3 models in  $M_{\text{vir}} \sim 10^{12} M_{\odot}$  haloes (Figs. 7 and 8). This is largely driven by the higher metallicity of the FIRE-2 CGM (Fig. 5).
- When comparing CGM observations to simulation and model predictions, it is important to account for the large uncertainties in halo masses estimated from galaxy stellar masses  $\gtrsim 10^{10.5} M_{\odot}$ . The main source of this uncertainty is scatter in the stellar-mass-halo-mass relation (Fig. A1).
- At these galaxy stellar masses  $\gtrsim 10^{10.5} M_{\odot}$ , there is a meaningful difference between halo masses calculated from the median halo mass at a given stellar mass (which we want), and from the median stellar mass at a given halo mass (Fig. A3). We show how to calculate halo masses from stellar masses in Appendix A.
- Compared to the observations of [Burchett et al. \(2019\)](#) and [Qu et al. \(2023\)](#), the Ne VIII column densities predicted with the FIRE physics models we studied are systematically low (Figs. 7 and 8). The FIRE-2 noBH model comes closest to the highest measured column densities, but the small number of haloes we study and the small number of available measurements preclude any strong conclusions. Other cosmological simulations also predict column densities below the higher measured values.

The highest measured column densities can be produced in a simple power-law CGM model, if we assume (very) high CGM warm/hot gas fractions and a high metallicity. These measurements therefore do not challenge our basic understanding of possible CGM masses and metallicities. However, it might be difficult to produce sufficiently high Ne VIII column densities in hydrodynamical simulations which self-consistently produce CGM properties along with realistic galaxies. This points to possible difficulties correctly and self-consistently modeling feedback and the baryon cycle in galaxies and their haloes. It also means that observations of the warm/hot CGM can help constrain these feedback models.

Observational issues could also be a factor in the difference between simulations and observations. For example, the area of the spectrum where Ne VIII is detected is crowded, complicating measurements, and galaxies undetected in the galaxy survey along the quasar sightlines could cause or contribute to absorption systems.

As they become available, a larger set of simulated haloes and/or measured absorbers could improve the robustness of these comparisons. We have also not used all the information in the observations: [Burchett et al. \(2019\)](#) and [Qu et al. \(2023\)](#) also measure the velocities of their absorption systems as a whole, and their component velocities. This kinematic and spatial information will contain information on ongoing gas flows, as well as the current warm/hot halo gas content. We intend to study these absorber kinematics in future work.

## DATA AVAILABILITY

A number of the FIRE-2 simulations analysed here are publicly available at <http://flathub.flatironinstitute.org/fire> ([Wetzel et al. 2023](#)). Additional data, including initial conditions and derived data products, are available at <https://fire.northwestern.edu/data/>. A public version of the GIZMO code is available at <http://www.tapir.caltech.edu/~phopkins/Site/GIZMO.html>. The scripts used to analyse the simulations will be made available on GITHUB if/when the paper is accepted for pub-

lication. Data shown in the plots is available on reasonable request to the authors.

## ACKNOWLEDGEMENTS

We thank Zhijie Qu and Hsiao-Wen Chen for sharing their CUBS data, and Phil Hopkins for helpful comments. N.A.W. was supported by a CIERA Postdoctoral Fellowship. C.-A.F.-G. was supported by NSF through grants AST-2108230 and CAREER award AST-1652522; by NASA through grants 17-ATP17-0067 and 21-ATP21-0036; by STScI through grant HST-GO-16730.016-A; and by CXO through grant TM2-23005X. L.B. was supported by the DOE Computer Science Graduate Fellowship through grant DE-SC0020347. I.S. was supported by the NSF Graduate Research Fellowship under Grant No. DGE-2234667.

The authors acknowledge the Texas Advanced Computing Center (TACC; <http://www.tacc.utexas.edu>) at The University of Texas at Austin for providing HPC resources that have contributed to the research results reported within this paper. In particular, we made use of the Frontera and Stampede2 systems, which are funded by the National Science Foundation (awards #1818253 and ACI-1540931, respectively). This research was supported in part through the computational resources and staff contributions provided for the Quest high performance computing facility at Northwestern University which is jointly supported by the Office of the Provost, the Office for Research, and Northwestern University Information Technology. The SMDPL simulation and halo finding has been performed at LRZ Munich within the project pr87yi. The CosmoSim database ([www.cosmosim.org](http://www.cosmosim.org)) providing the file access is a service by the Leibniz-Institute for Astrophysics Potsdam (AIP).

We made use of PYTHON and C code for this analysis. In particular, we used the following PYTHON modules: ASTROPY (Astropy Collaboration et al. 2013, 2018, 2022), H5PY (Collette 2013), MATPLOTLIB (Hunter 2007), NUMPY (Harris et al. 2020), PANDAS (The pandas development team 2020; Wes McKinney 2010), and SCIPY (Virtanen et al. 2020), and the IPYTHON command-line interface (Pérez & Granger 2007).

## REFERENCES

- Asplund M., Grevesse N., Sauval A. J., Scott P., 2009, *Annual Review of Astronomy and Astrophysics*, 47, 481
- Astropy Collaboration et al., 2013, *A&A*, 558, A33
- Astropy Collaboration et al., 2018, *aj*, 156, 123
- Astropy Collaboration et al., 2022, *apj*, 935, 167
- Babik I. V., McNamara B. R., Nulsen P. E. J., Russell H. R., Vantghem A. N., Hogan M. T., Pulido F. A., 2018, *ApJ*, 862, 39
- Barret D., et al., 2018, in *Space Telescopes and Instrumentation 2018: Ultraviolet to Gamma Ray*. p. 106991G ([arXiv:1807.06092](https://arxiv.org/abs/1807.06092)), doi:10.1117/12.2312409
- Behroozi P. S., Wechsler R. H., Wu H.-Y., 2013a, *ApJ*, 762, 109
- Behroozi P. S., Wechsler R. H., Wu H.-Y., Busha M. T., Klypin A. A., Primack J. R., 2013b, *ApJ*, 763, 18
- Behroozi P., Wechsler R. H., Hearin A. P., Conroy C., 2019, *MNRAS*, 488, 3143
- Branchini E., et al., 2009, *ApJ*, 697, 328
- Bregman J. N., Lloyd-Davies E. J., 2007, *ApJ*, 669, 990
- Bryan G. L., Norman M. L., 1998, *ApJ*, 495, 80
- Burchett J. N., et al., 2016, *ApJ*, 832, 124
- Burchett J. N., et al., 2019, *ApJ*, 877, L20
- Cen R., Fang T., 2006, *ApJ*, 650, 573
- Chan T. K., Kereš D., Hopkins P. F., Quataert E., Su K. Y., Hayward C. C., Faucher-Giguère C. A., 2019, *MNRAS*, 488, 3716
- Chen X., Weinberg D. H., Katz N., Davé R., 2003, *ApJ*, 594, 42
- Chen H.-W., et al., 2020, *MNRAS*, 497, 498
- Colbrook M. J., Ma X., Hopkins P. F., Squire J., 2017, *MNRAS*, 467, 2421
- Collette A., 2013, Python and HDF5. O'Reilly, Sebastopol CA, USA, <http://www.h5py.org/>
- Crain R. A., et al., 2015, *MNRAS*, 450, 1937
- Cui W., et al., 2020, *Journal of Low Temperature Physics*, 199, 502
- Das S., Mathur S., Gupta A., Nicastro F., Krongold Y., 2019, *ApJ*, 887, 257
- Davies J. J., Crain R. A., Oppenheimer B. D., Schaye J., 2020, *Monthly Notices of the Royal Astronomical Society*, 491, 4462
- Dutton A. A., Macciò A. V., 2014, *MNRAS*, 441, 3359
- Faerman Y., Pandya V., Somerville R. S., Sternberg A., 2022, *ApJ*, 928, 37
- Faucher-Giguère C.-A., 2020, *MNRAS*, 493, 1614
- Faucher-Giguère C.-A., Oh S. P., 2023, *arXiv e-prints*, p. [arXiv:2301.10253](https://arxiv.org/abs/2301.10253)
- Faucher-Giguère C.-A., Lidz A., Zaldarriaga M., Hernquist L., 2009, *ApJ*, 703, 1416
- Ford A. B., Oppenheimer B. D., Davé R., Katz N., Kollmeier J. A., Weinberg D. H., 2013, *MNRAS*, 432, 89
- Garrison-Kimmel S., et al., 2017, *MNRAS*, 471, 1709
- Garrison-Kimmel S., et al., 2019, *MNRAS*, 487, 1380
- Gupta A., Mathur S., Galeazzi M., Krongold Y., 2014, *Ap&SS*, 352, 775
- Gupta A., Mathur S., Krongold Y., 2017, *ApJ*, 836, 243
- Hafen Z., et al., 2019, *MNRAS*, 488, 1248
- Hafen Z., et al., 2020, *MNRAS*, 494, 3581
- Harris C. R., et al., 2020, *Nature*, 585, 357
- Hellsten U., Gnedin N. Y., Miralda-Escudé J., 1998, *ApJ*, 509, 56
- Hopkins P. F., 2015a, *MNRAS*, 450, 53
- Hopkins P. F., 2015b, *MNRAS*, 450, 53
- Hopkins P. F., 2016, *MNRAS*, 462, 576
- Hopkins P. F., 2023, *MNRAS*, 518, 5882
- Hopkins P. F., Raives M. J., 2016, *MNRAS*, 455, 51
- Hopkins P. F., Quataert E., Murray N., 2012, *MNRAS*, 421, 3488
- Hopkins P. F., Torrey P., Faucher-Giguère C.-A., Quataert E., Murray N., 2016, *MNRAS*, 458, 816
- Hopkins P. F., et al., 2018a, *MNRAS*, 477, 1578
- Hopkins P. F., et al., 2018b, *MNRAS*, 480, 800
- Hopkins P. F., et al., 2020, *MNRAS*, 492, 3465
- Hopkins P. F., Squire J., Butsky I. S., 2022a, *MNRAS*, 509, 3779
- Hopkins P. F., Butsky I. S., Panopoulou G. V., Ji S., Quataert E., Faucher-Giguère C.-A., Kereš D., 2022b, *MNRAS*, 516, 3470
- Hopkins P. F., Squire J., Butsky I. S., Ji S., 2022c, *MNRAS*, 517, 5413
- Hopkins P. F., et al., 2023, *MNRAS*, 519, 3154
- Hunter J. D., 2007, *Computing in Science & Engineering*, 9, 90
- Ji S., et al., 2020, *MNRAS*, 496, 4221
- Klypin A., Yepes G., Gottlöber S., Prada F., Heß S., 2016, *MNRAS*, 457, 4340
- Kraft R., et al., 2022, *arXiv e-prints*, p. [arXiv:2211.09827](https://arxiv.org/abs/2211.09827)
- Kroupa P., 2001, *Monthly Notices of the Royal Astronomical Society*, 322, 231
- Leitherer C., et al., 1999, *ApJS*, 123, 3
- Liang C. J., Kravtsov A. V., Agertz O., 2016, *MNRAS*, 458, 1164
- Martizzi D., Faucher-Giguère C.-A., Quataert E., 2015, *MNRAS*, 450, 504
- McQuinn M., 2014, *ApJ*, 780, L33
- Miller M. J., Bregman J. N., 2015, *ApJ*, 800, 14
- Mitchell P. D., Schaye J., 2022, *MNRAS*, 511, 2948
- Moster B. P., Naab T., White S. D. M., 2013, *MNRAS*, 428, 3121
- Mroczkowski T., et al., 2019, *Space Sci. Rev.*, 215, 17
- Muratov A. L., Kereš D., Faucher-Giguère C.-A., Hopkins P. F., Quataert E., Murray N., 2015, *MNRAS*, 454, 2691
- Muratov A. L., et al., 2017, *MNRAS*, 468, 4170
- Nandra K., et al., 2013, *arXiv e-prints*, p. [arXiv:1306.2307](https://arxiv.org/abs/1306.2307)
- Navarro J. F., Frenk C. S., White S. D. M., 1997, *ApJ*, 490, 493
- Nelson D., et al., 2023, *MNRAS*, 522, 3665
- Nicastro F., 2016, in *XMM-Newton: The Next Decade*. p. 27 ([arXiv:1611.03722](https://arxiv.org/abs/1611.03722))
- Pandya V., et al., 2020, *ApJ*, 905, 4



- Pérez F., Granger B. E., 2007, *Computing in Science & Engineering*, 9, 21
- Perna R., Loeb A., 1998, *ApJ*, 503, L135
- Ploetckinger S., Schaye J., 2020, *MNRAS*, 497, 4857
- Power C., Navarro J. F., Jenkins A., Frenk C. S., White S. D. M., Springel V., Stadel J., Quinn T., 2003, *MNRAS*, 338, 14
- Prochaska J. X., et al., 2019, *ApJS*, 243, 24
- Qu Z., Bregman J. N., 2018, *ApJ*, 856, 5
- Qu Z., Chen H.-W., et al., 2023, in prep., ???, ???
- Ravi V., 2019, *ApJ*, 872, 88
- Rodríguez-Puebla A., Behroozi P., Primack J., Klypin A., Lee C., Hellinger D., 2016, *MNRAS*, 462, 893
- Samuel J., et al., 2020, *MNRAS*, 491, 1471
- Schaye J., et al., 2015, *MNRAS*, 446, 521
- Smith R. K., et al., 2016, in *Space Telescopes and Instrumentation 2016: Ultraviolet to Gamma Ray*, Society of Photo-Optical Instrumentation Engineers (SPIE), Bellingham, Washington USA, p. 99054M, doi:10.1117/12.2231778
- Stern J., Fielding D., Faucher-Giguère C.-A., Quataert E., 2019, *MNRAS*, 488, 2549
- Su K.-Y., et al., 2021, *MNRAS*, 507, 175
- The EAGLE team 2017, arXiv e-prints, p. arXiv:1706.09899
- The Lynx Team 2018, arXiv e-prints,
- The pandas development team 2020, pandas-dev/pandas: Pandas, doi:10.5281/zenodo.3509134, https://doi.org/10.5281/zenodo.3509134
- Torrey P., et al., 2020, *MNRAS*, 497, 5292
- Tripp T. M., et al., 2011, *Science*, 334, 952
- Tumlinson J., Peebles M. S., Werk J. K., 2017, *ARA&A*, 55, 389
- Verner D. A., Tytler D., Barthel P. D., 1994, *ApJ*, 430, 186
- Virtanen P., et al., 2020, *Nature Methods*, 17, 261
- Voit G. M., 2019, *ApJ*, 880, 139
- Wellons S., et al., 2023, *MNRAS*, 520, 5394
- Wendland H., 1995, *Advances in Computational Mathematics*, 4, 389
- Werk J. K., et al., 2014, *ApJ*, 792, 8
- Wes McKinney 2010, in *Stéfan van der Walt Jarrod Millman eds, Proceedings of the 9th Python in Science Conference*. pp 56 – 61, doi:10.25080/Majorsa-92bf1922-00a
- Wetzel A. R., Hopkins P. F., Kim J.-h., Faucher-Giguère C.-A., Kereš D., Quataert E., 2016, *ApJ*, 827, L23
- Wetzel A., et al., 2023, *ApJS*, 265, 44
- Wiersma R. P. C., Schaye J., Smith B. D., 2009, *MNRAS*, 393, 99
- Wijers N. A., Schaye J., 2022, *MNRAS*, 514, 5214
- Wijers N. A., Schaye J., Oppenheimer B. D., 2020, *MNRAS*, 498, 574
- Zhu Z., et al., 2021, *ApJ*, 908, 17

## APPENDIX A: ESTIMATING HALO MASSES FROM STELLAR MASSES

Here, we explore some effects of different ways of calculating the halo mass from stellar mass. The effects are largest at central galaxy stellar masses of  $M_\star \gtrsim 10^{10.5} M_\odot$ . Using a typical halo mass at a given stellar masses, and not a typical stellar mass at a given halo mass, to estimate halo masses is important. Furthermore, accounting for scatter in the stellar-mass-halo-mass relation is important for both the best-estimate halo masses and the halo mass uncertainty.

As discussed in §4.1.3, we use UniverseMachine central galaxy and halo catalogues in our analysis. In Fig. A1, we show the distribution of the UniverseMachine stellar and halo masses for central galaxies. The colored lines show relations between stellar mass and halo mass. At galaxy stellar masses  $M_\star \gtrsim 10^{10.5} M_\odot$ , the Burchett et al. (2016, 2019) relation differs quite a lot from the median halo mass at a given stellar mass. The scatter in halo mass at fixed stellar mass is also considerable, especially at  $M_\star \gtrsim 10^{10.5} M_\odot$ .

Burchett et al. (2016) used the stellar-mass-halo-mass relation of Moster et al. (2013) as a starting point for their relation. Moster et al.

(2013) fit a the ratio of stellar mass to halo mass, as a function of halo mass, using a double power law function. This means that they are considering the typical stellar mass at a given halo mass, not the typical halo mass at a given stellar mass. There is a sizeable difference between those two curves at  $M_\star \gtrsim 10^{10.5} M_\odot$  in our redshift range of interest ( $z = 0.5-1$ ).

Burchett et al. (2016) noted that the halo masses obtained by inverting the Moster et al. (2013) stellar mass as a function of halo mass were too high at high halo masses: the halo masses were of groups and clusters, not the isolated galaxies they observed. They argued a flatter slope at high galaxy masses was more appropriate for their isolated galaxies.

We argue that these differences are most likely explained by the difference between the typical halo mass at a given stellar mass, and a mathematically inverted typical stellar mass as a function of halo mass. These differences are the result of scatter in the stellar-mass-halo-mass relation, combined with the fact that high-mass haloes and galaxies are considerably rarer than lower-mass systems. However, we note that the flatter Burchett et al. (2016) slope at high stellar masses reasonably matches the median halo mass at a given stellar mass up to almost  $M_\star \approx 10^{11} M_\odot$ , which is above the  $M_\star \approx 10^{10.5} M_\odot$  where the  $M_\star(M_{\text{vir}})$  and  $M_{\text{vir}}(M_\star)$  median relations diverge.

All in all, it is clear that, especially at high stellar masses, which relation between stellar mass and halo mass ones uses can have a big effect on the halo mass retrieved.

Fig. A1 also shows that the uncertainty in halo mass at a given stellar mass is large, again, especially at  $M_\star \gtrsim 10^{10.5} M_\odot$ . We illustrate the uncertainty in the halo masses in Fig. A2. Here, we calculate the halo mass for a given galaxy using the stellar masses and their uncertainties as reported by Burchett et al. (2019). In particular, we take the galaxies listed in their table 1, which are those for which they have either measured one or more Ne VIII absorption lines (blue curves), or those within 450 pkpc (impact parameter) of their line of sight for which they obtained upper limits instead (orange, more transparent curves). We take their reported log stellar masses and uncertainties, and assume the probability distribution for the true log stellar mass is a gaussian distribution with the best-estimate stellar mass as the mean and the uncertainty as the variance.

We then use the distribution of halo masses at a given stellar mass in the UniverseMachine catalog to translate these to probability distributions for parent halo masses. The probability for a given halo mass bin is

$$P(M_h \in [M_{h,j}, M_{h,j+1}]) = \sum_i \{P(M_\star \in [M_{\star,i}, M_{\star,i+1}]) \cdot P(M_h \in [M_{h,j}, M_{h,j+1}] | M_\star \in [M_{\star,i}, M_{\star,i+1}])\}, \quad (\text{A1})$$

where  $M_{h,j}$  and  $M_{\star,i}$  are edges of bins in halo and stellar mass, respectively. For the probabilities  $P(M_h | M_\star)$ , we simply use a normalized histogram of the UniverseMachine stellar and halo masses. We note that there are further (systematic) uncertainties associated with the measurement of stellar masses, which we do not account for here. As the relation depends on redshift, we use the halo catalog for the redshift closest to the measured galaxy redshift.

We calculate the Qu et al. (2023) halo masses in the same way as the Burchett et al. (2019) masses. However, the estimated probability distribution for the true stellar mass of a galaxy is a bit more complicated. Qu et al. (2023) report different lower and upper error ranges for the stellar masses of some galaxies. The errors they report are  $2\sigma$ . We therefore approximate the true stellar mass probability distribution for a measured galaxy as two half lognormal distributions



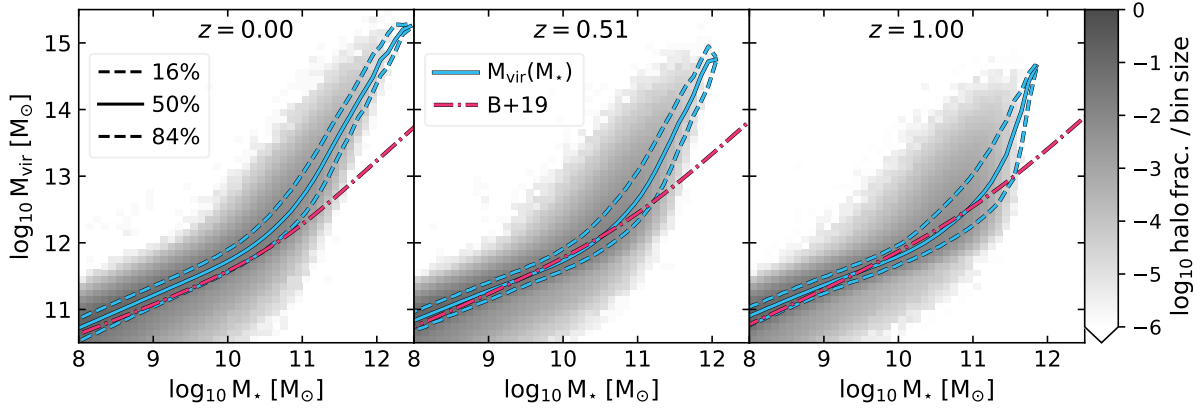


**Figure A1.** A histogram of the joint (central galaxy) stellar and halo mass distribution (grayscale), taken from the UniverseMachine abundance-matching fits applied to the SMDPL simulations. The cyan lines show different percentiles of  $M_{\text{vir}}(M_*)$ , the halo mass as a function of stellar mass, for the UniverseMachine galaxies. The red curve shows a modified version of the [Moster et al. \(2013\)](#) relation, introduced by [Burchett et al. \(2016\)](#) and used by [Burchett et al. \(2019\)](#) to calculate the virial radii in their table 1. We convert the [Burchett et al. \(2019\)](#)  $M_{200c}$  halo masses to the [Bryan & Norman \(1998\)](#) definition assuming their mass profiles are NFW ([Navarro et al. 1997](#)), with concentrations following [Dutton & Macciò \(2014\)](#). Different relations give different halo masses for a measured stellar mass, and the scatter in halo mass at fixed stellar mass can be large. The differences and scatter are largest at  $M_* \gtrsim 10^{10.5} M_\odot$ .

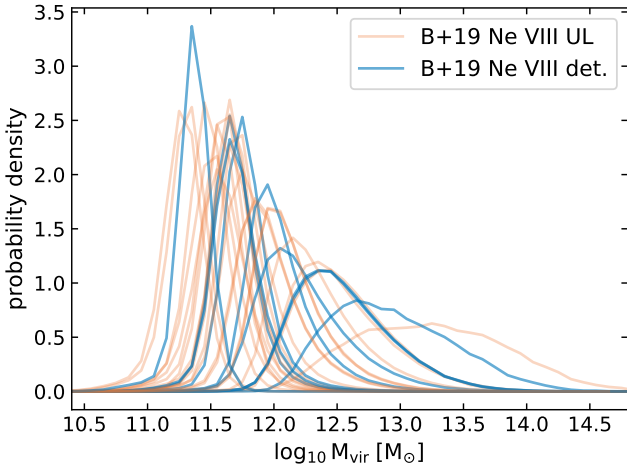


**Figure A2.** Probability distributions for the parent halo masses ([Bryan & Norman 1998](#), definition) of the galaxies for which [Burchett et al. \(2019\)](#) measured Ne VIII column densities (det., blue curves) and upper limits (UL, orange and more transparent curves). These distributions were obtained assuming a gaussian probability distribution of log stellar mass, with mean and variance taken from tab. 1 of [Burchett et al. \(2019\)](#). More details on the method are given in the text. The halo masses for the higher-mass haloes in this sample are highly uncertain, by up to  $\sim 1$  dex. This makes it difficult to fairly compare them to simulated haloes.

(each with a total probability of 0.5), centered at the measured value and with a variance equal to the upper/lower uncertainty. We estimate the  $1\sigma$  upper/lower uncertainty  $\sigma_{\text{tot}}$  by combining the reported statistical uncertainty and the systematic uncertainty  $\sigma_{\text{sys}}$  of 0.2 dex of the stellar mass measurements. We estimate the  $1\sigma$  statistical uncertainty as half the reported  $2\sigma$  statistical uncertainties  $\sigma_{2,\text{stat}}$ . This means the variance of each half-lognormal distribution is estimated as  $\sigma_{\text{tot}}^2 = \sqrt{(\sigma_{2,\text{stat}}^2 / 4 + \sigma_{\text{sys}}^2)}$ .

Using the UniverseMachine distribution of halo masses at a given stellar mass, we can reasonably estimate the halo masses of lower-mass systems, but at higher stellar and halo masses, the halo mass

estimates become highly uncertain. These wide ranges of possible halo masses result from the combination of scatter with a steep slope in  $M_{\text{vir}}(M_*)$ . This makes it difficult to compare the simulated CGM to CGM observations based on matching observationally inferred halo masses. Matching stellar masses is possible, in principle, but we believe the halo mass is more important than the galaxy stellar mass in determining the properties of the warm-hot CGM.

In Fig. A3 we calculate likely halo masses for a few representative galaxy stellar masses and uncertainties from [Burchett et al. \(2019\)](#). Different line styles are for different galaxies, different colors are for different relations. The teal curves use the same method as in Fig. A2, except that we assume a single redshift  $z = 0.74$ , in the middle of our range of interest, for this example. The probability distributions come from assuming a gaussian distribution for the log stellar masses.

For the teal curves, we calculate the halo mass probability density according to eq. A1: we calculate the probability for a given halo mass simply by normalizing the UniverseMachine halo mass distribution in a given stellar mass bin to one. We then multiply these distributions by the probability for each stellar mass bin (given its measurement and error) and add the results in each halo mass bin to obtain the probability that the halo mass falls in that bin.

For the cyan curve, we used a similar method, but ignored errors in the stellar mass measurements. Instead, the probability distribution is just the normalized halo mass histogram at the best-estimate stellar mass. The blue curve effectively does the opposite: we include uncertainties in the true stellar mass, but ignore scatter in the SMHM relation. Here, we still start with a probability for different stellar mass bins. However, we simply convert the stellar mass bin edges to halo mass bin edges using the median halo mass at a given stellar mass. The probabilities remain the same, and we simply divide by the resulting halo mass bin sizes to obtain the probability density. Markers on the blue curves show the halo mass corresponding to the best-estimate stellar mass.

Comparing the blue and cyan curves to the teal, we see that the uncertainty in the halo masses largely comes from the scatter in the SMHM at all these masses. However, the SMHM scatter is a more dominant error source at high stellar and halo masses. At masses  $M_* \gtrsim 10^{10.5} M_\odot$ , obtaining the most likely halo masses also requires

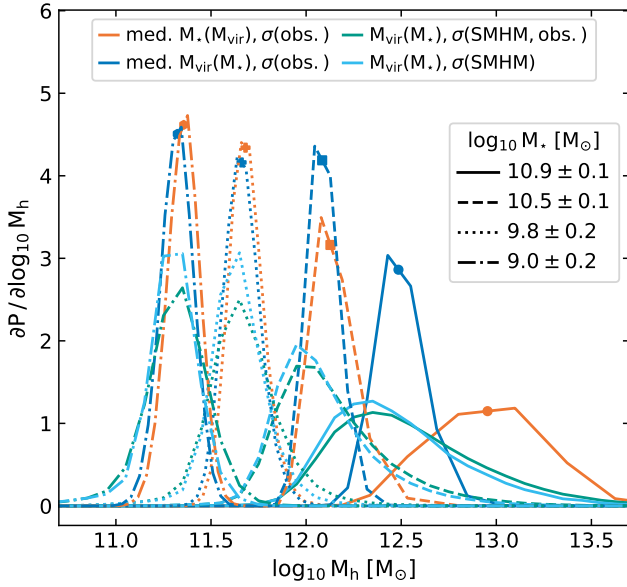


**Figure A3.** Probability densities for host halo masses of galaxies with different stellar masses (different line styles) from [Burchett et al. \(2019\)](#), assuming a redshift  $z = 0.74$ . The curves of different colors represent different methods for calculating the halo mass at a given stellar mass. The teal curves show halo mass probability densities calculated from the probabilities of different true stellar masses (given the measurement and its error), and the probabilities of different halo masses at each stellar mass. The cyan curves instead account only for the scatter in the stellar-mass-halo-mass relation: these give the halo mass probability distributions only for the best-estimate stellar mass. The blue curves instead only account for uncertainty in the measured stellar mass. We take the median halo mass for the stellar mass at the edge of each mass bin, and then simply assign the same probabilities to the resulting halo mass bins as the original stellar mass bins. (We do divide by the size of the halo mass bins to obtain the probability density.) The orange curves are obtained in the same way as the blue curves, except that we use the wrong stellar-mass-halo-mass relation: we mathematically invert the median stellar mass as a function of halo mass, simply by linearly interpolating between the median stellar masses. The uncertainties are again simply calculated by applying the relation to stellar mass bin edges.

accounting for the SMHM scatter, although at lower masses, the median relation suffices for this.

The orange curves show a method of calculating the halo masses which we strongly caution against. The approach is similar to that of the blue curve, using a one-to-one relation between halo mass and stellar mass, and simply propagating the uncertainties in the stellar mass through that relation to obtain the uncertainties in the halo mass. However, here, we use the median *stellar* mass at a given *halo* mass to define the relation. We calculate median log stellar masses over a range of log halo masses, and simply linearly interpolate between the resulting points to obtain the halo mass at a given stellar mass.

At low stellar masses ( $\lesssim 10^{10.5} M_{\odot}$ ), this provides reasonable best-estimate halo masses. The lack of inclusion of SMHM scatter does lead to an underestimate of the halo mass uncertainty, but the distributions are very similar to those obtained using the appropriate relation, median halo mass at a given stellar mass. However, at higher stellar masses ( $\gtrsim 10^{10.5} M_{\odot}$ ), the median stellar mass at a given halo mass yields considerably higher halo mass estimates than the median halo mass at a given stellar mass. At these masses, it is important to both use the correct relation, and to account for SMHM scatter.

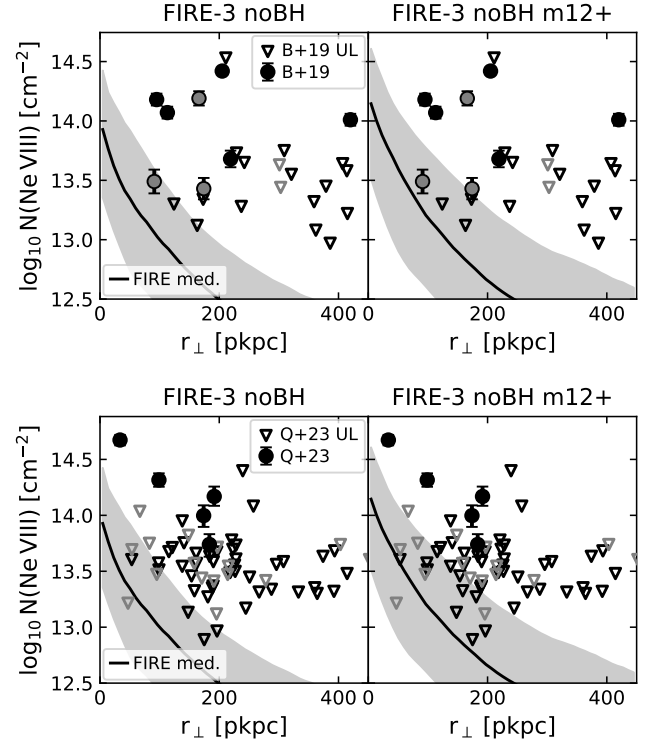


**Figure B1.** A comparison of the m12 FIRE-3 noBH haloes to the [Burchett et al. \(2019\)](#) data (top panels) and the [Qu et al. \(2023\)](#) data (bottom panels). Like Figs. 7 and 8, the solid lines show the median for the FIRE models across m12 haloes and redshifts 0.5, 0.6, 0.7, 0.8, 0.9, and 1.0. Here, we compare the FIRE-3 noBH sample from the main body of the paper to the FIRE-3 noBH m12+ sample listed in Tab. B1. Including m12 haloes with higher halo and stellar masses improves the agreement with the data somewhat, but most measured column densities are still underpredicted.

In short, different in-use stellar-mass-halo-mass relations can lead to major differences in halo mass inferred for a given stellar mass, especially if a galaxy is  $\gtrsim L_{*}$ . The scatter in halo mass at fixed stellar mass means that, besides these systematic uncertainties, there are large statistical uncertainties in the halo mass for a given stellar mass ( $> 0.5$  dex at  $M_{*} \sim 10^{11} M_{\odot}$ ).

## APPENDIX B: M12 FIRE-3 NOBH HALOES WITH HIGHER HALO MASSES

In the main body of the paper, we analysed samples of m12 haloes with similar halo masses for the four different physics models we explored. However, these halo masses correspond to different central galaxy stellar masses in the different FIRE models. In particular, the FIRE-2 noBH model produces higher central galaxy stellar masses in its m12 haloes than the FIRE-3 models.

After the simulations in the main body of this paper were run, additional m12 galaxies were simulated with the FIRE-3 noBH model. Some of these have higher halo masses than our main m12 FIRE-3 noBH sample, and central galaxy stellar masses comparable to those of our FIRE-2 noBH halo sample. These haloes are listed in Tab. B1.

Here, we test if the difference in central galaxy stellar masses might explain the column density difference between the FIRE-2 noBH and FIRE-3 noBH m12 haloes. In Fig. B1, we compare to

**Table B1.** As Table 1, but for an additional set of m12 FIRE-3 noBH haloes, some of which have higher halo and stellar masses than the FIRE-3 noBH sample we analyse in the main body of this work. Three of these haloes have resolutions matching those of our other m12 FIRE-3 noBH haloes, the other nine were run at lower resolution.

ICs	model	resolution [M <sub>⊙</sub> ]	M <sub>vir</sub> [M <sub>⊙</sub> ]	z = 1.0			z = 0.5		
				M <sub>★</sub> [M <sub>⊙</sub> ]	R <sub>vir</sub> [pkpc]	M <sub>vir</sub> [M <sub>⊙</sub> ]	M <sub>★</sub> [M <sub>⊙</sub> ]	R <sub>vir</sub> [pkpc]	
m12a	FIRE-3 noBH	6e4	8.3e11	1.1e10	146	1.2e12	2.3e10	211	
m12d	FIRE-3 noBH	6e4	5.2e11	5.1e9	124	7.0e11	9.7e9	175	
m12e	FIRE-3 noBH	6e4	1.0e12	2.8e9	157	1.4e12	5.6e9	221	
m12g	FIRE-3 noBH	6e4	1.7e12	1.7e10	186	1.9e12	4.5e10	245	
m12j	FIRE-3 noBH	6e4	2.8e11	1.7e9	102	7.1e11	4.8e9	176	
m12j	FIRE-3 noBH	7e3	3.1e11	1.9e9	105	7.1e11	9.1e9	176	
m12k	FIRE-3 noBH	6e4	1.2e12	1.2e10	166	1.9e12	2.5e10	245	
m12n	FIRE-3 noBH	6e4	7.8e11	2.1e9	143	8.9e11	5.8e9	190	
m12n	FIRE-3 noBH	7e3	8.3e11	1.3e10	146	9.3e11	1.5e10	193	
m12u	FIRE-3 noBH	3e4	5.5e11	1.7e9	127	5.2e11	4.3e9	158	
m12x	FIRE-3 noBH	3e4	2.7e11	1.6e9	100	5.0e11	2.4e9	157	
m12x	FIRE-3 noBH	4e3	2.6e11	1.1e9	98	4.1e11	1.4e9	147	

good and plausible halo-mass-matched data points in the same way as in §4, but we base the halo mass selection range on the range of halo masses in the combined m12 FIRE-3 noBH sample.

We find that the lower stellar masses in the FIRE-3 noBH m12 haloes might play a part in their lower column densities relative to the FIRE-2 noBH haloes. However, the stellar masses do not fully explain the differences (Fig. B1).

We note that these differences, along with the fairly large uncertainties on the observed halo masses, mean that the comparisons we make between simulations and observations include some systematic uncertainties on how to match the two samples.

### APPENDIX C: THE POWER-LAW CGM MODEL

For our simple power law CGM model, we assume a spherically symmetrical gas distribution within a dark-matter-dominated potential well. We assume power-law circular velocity ( $v_c$ ) and entropy ( $K$ ) profiles

$$v_c \propto r^m, \quad (C1)$$

$$K \propto r^l, \quad (C2)$$

where  $r$  is the distance to the halo center, and  $m$  and  $l$  are the exponents of the circular velocity and entropy profiles, respectively. The entropy is defined as  $K = kTn^{-2/3}$ , where  $k$  is the Boltzmann constant, and  $n$  is the gas particle number density.

Following Stern et al. (2019), we assume a steady-state inflow within this halo. If the only relevant forces are gravity and gas pressure, Newton's second law applied to a gas element gives

$$\rho V \frac{d^2 r}{dt^2} = -V \frac{dP}{dr} - \rho V \frac{GM(<r)}{r^2}, \quad (C3)$$

where  $\rho$  is density,  $V$  is volume,  $t$  is time,  $P$  is pressure,  $G$  is Newton's constant, and  $M(<r)$  is the enclosed mass within radius  $r$ . Using  $v_c = \sqrt{GM(<r)}/r$  and the fact that velocity depends only on radius (and not explicitly on time) in this model, we obtain

$$\frac{1}{2} \frac{dv_c^2}{dr} = -\frac{1}{\rho} \frac{dP}{dr} - \frac{v_c^2}{r}, \quad (C4)$$

which is eq. 2 of Stern et al. (2019). Following Stern et al. (2019), we

multiply by  $r/c_s^2$ , where  $c_s = \sqrt{\gamma P/\rho}$  is the adiabatic sound speed and  $\gamma$  is the adiabatic index. This gives

$$\mathcal{M}^2 \frac{d \ln v}{d \ln r} = -\frac{1}{\gamma} \frac{d \ln P}{d \ln r} - \frac{v_c^2}{c_s^2}, \quad (C5)$$

where  $\mathcal{M} = v/c_s$  is the Mach number. This is eq. 16 of Stern et al. (2019). From here, we make another assumption: that the inflows are subsonic, i.e.,  $\mathcal{M} \ll 1$ . Setting the left-hand term of equation C5 to zero, we then obtain

$$-\frac{1}{\gamma} \frac{d \ln P}{d \ln r} = \frac{v_c^2}{c_s^2}. \quad (C6)$$

We further assume that the CGM gas is a monatomic ideal gas, meaning  $\gamma = 5/3$ .

Since we are assuming the thermodynamical quantities follow power laws,  $d \ln P / d \ln r$  is a constant, meaning  $v_c^2 / c_s^2$  must be as well. Since  $c_s^2 = \gamma kT / \mu m_H$ , where  $T$  is the temperature and  $\mu$  in the mean molecular mass in units of the hydrogen atom mass  $m_H$ ,

$$T \propto c_s^2 \propto v_c^2 \propto r^{2m}. \quad (C7)$$

We have assumed here that the mean molecular mass  $\mu$  is constant. This is reasonable for the warm/hot CGM, where hydrogen and helium are fully ionized, and electron contributions from metals are small.

We can then also solve for the density slope using the entropy, and again assuming  $\rho/n = \mu m_H$  is constant. Since  $K = kTn^{-2/3}$ , we get

$$l = \frac{d \ln K}{d \ln r} = \frac{d \ln T}{d \ln r} - \frac{2}{3} \frac{d \ln \rho}{d \ln r} = 2m - \frac{2}{3} \frac{d \ln \rho}{d \ln r}, \quad (C8)$$

which means

$$\rho \propto r^{-3l/2+3m}. \quad (C9)$$

Finally, this also gives the pressure slope, which is simply the sum of the temperature and density slopes. We use this to solve eq. C6 for the sound speed

$$\frac{v_c^2}{c_s^2} = -3m + \frac{9}{10}l. \quad (C10)$$

This gives the normalization of the temperature profile. Using

$$T_{\text{vir}} = \frac{\mu m_H v_c(R_{\text{vir}})}{2k}, \quad (C11)$$

where  $T_{\text{vir}}$  is the virial temperature and  $R_{\text{vir}}$  is the virial radius, we get

$$T(R_{\text{vir}}) = \frac{6}{5} \frac{1}{\frac{9}{10}l - 3m} T_{\text{vir}}. \quad (\text{C12})$$

If we chose the entropy slope to be  $l = 1 + 4m / 3$ , we recover the power-law cooling-flow solution of [Stern et al. \(2019\)](#).

The normalization of the density profile does not follow from the assumptions we have made above. We set this normalization by requiring that the mass of this CGM gas (within  $R_{\text{vir}}$ ) is the cosmic baryon fraction (or some fraction thereof) of the halo mass  $M_{\text{vir}}$ .

This paper has been typeset from a  $\text{\TeX}/\text{\LaTeX}$  file prepared by the author.